Assimilation of Water Vapor Retrievals from Z_{DR} Columns Using the 3DVar Method for Improving the Short-Term Prediction of Convective Storms

HAIQIN CHEN,[a,b,c] JIDONG GAO,[f] TAO SUN,[g] YAODENG CHEN,[d] YUNHENG WANG,[e,f] AND JACOB T. CARLIN[e,f]

[a] *School of Meteorology, Nanjing University, Nanjing, China*
[b] *China Meteorological Administration Tornado Key Laboratory, Foshan, China*
[c] *State Key Laboratory of Severe Weather and Key Laboratory of Radar Meteorologyy, China Meteorology Administration, Beijing, China*
[d] *Key Laboratory of Meteorological Disaster of Ministry of Education (KLME), Collaborative Innovation Center on Forecast and Evaluation of Meteorological Disasters (CIC-FEMD), Nanjing University of Information Science and Technology, Nanjing, China*
[e] *Cooperative Institute for Severe and High-Impact Weather Research and Operations, University of Oklahoma, Norman, Oklahoma*
[f] *NOAA/OAR/National Severe Storms Laboratory, Norman, Oklahoma*
[g] *National Center for Atmospheric Research, Boulder, Colorado*

(Manuscript received 7 September 2023, in final form 29 January 2024, accepted 1 February 2024)

ABSTRACT: The differential reflectivity (Z_{DR}) column is a notable polarimetric signature related to updrafts in deep moist convection. In this study, pseudo–water vapor (q_v) observations are retrieved from observed Z_{DR} columns under the assumption that humidity is saturated within the convection where Z_{DR} columns are detected, and are then assimilated within the 3DVar framework. The impacts of assimilating pseudo-q_v observations from Z_{DR} columns on short-term severe weather prediction are first evaluated for a squall-line case. Radar data analysis indicates that the Z_{DR} columns are mainly located on the inflow side of the high-reflectivity region. Assimilation of the pseudo-q_v observations leads to an enhancement of q_v within the convection, while concurrently reducing humidity in no-rain areas. Sensitivity experiments indicate that a tuned smaller observation error and a shorter horizontal decorrelation scale are optimal for a better assimilation of pseudo-q_v from Z_{DR} columns, resulting in more stable rain rates during short-term forecasts. Additionally, a 15-min cycling assimilation frequency yields the best performance, providing the most accurate reflectivity forecast in terms of both location and intensity. Analysis of thermodynamic fields reveal that assimilating Z_{DR} columns provides more favorable initial conditions for sustaining convection, including sustainable moisture condition, a strong cold pool, and divergent winds near the surface, consequently enhancing reflectivity and precipitation. With the optimal configuration determined from the sensitivity tests, a quantitative evaluation further demonstrates that assimilating the pseudo-q_v observations from Z_{DR} columns using the 3DVar method can improve the 0–3-h reflectivity and accumulated precipitation predictions of convective storms.

KEYWORDS: Numerical weather prediction/forecasting; Cloud resolving models; Data assimilation

1. Introduction

Convective-scale severe weather, characterized by rapid evolution, high nonlinearity, and low predictability, causes significant loss of life and property worldwide each year. There has long been a focus on research and operational efforts to improve convective-scale numerical weather prediction (NWP). This improvement heavily depends on accurately representing fast-evolving convective storms in initial conditions through assimilating high-resolution observations at a high frequency. Radar data are among the most crucial observations in convective-scale data assimilation (DA), as they provide internal dynamic and microphysical information about storms with high temporal and spatial resolution. Much effort has been dedicated to assimilating radial velocity and reflectivity data from Doppler radar. It is widely acknowledged that assimilating radar data can effectively enhance short-term predictions of severe weather (see Sun et al. 2014; Gustafsson et al. 2018 for a review).

Compared to radial velocity, assimilating reflectivity presents greater challenges, in part because reflectivity is not typically a model state variable. This has prompted the exploration of various methods to optimally assimilate reflectivity data into NWP models. Two primary approaches can be used to assimilate reflectivity. Because radar reflectivity is determined in part by the size distribution of precipitation particles, assimilating hydrometeor contents directly related to reflectivity data is a natural choice. Some studies opt to directly assimilate reflectivity data to analyze hydrometeors by using a reflectivity observation operator. These operators convert hydrometeors from model space to the equivalent reflectivity in observation space, and can be used with either variational methods (Sun and Crook 1997; Xiao et al. 2007; Gao and Stensrud 2012; Wang and Wang 2017) or the Ensemble Kalman Filter (EnKF) method (Tong and Xue 2005; Xue et al. 2006, 2010). Other studies assimilate hydrometeors derived from reflectivity. This was initially attempted using the Local Analysis and Prediction Systems (LAPS; Albers et al. 1996), where hydrometeor classifications and updates within a 3D cloud region were based on the microphysical scheme. This method was later widely adopted by the Rapid Update Cycle (RUC; Benjamin et al. 2004) and High-Resolution Rapid Refresh (HRRR) (Smith et al. 2008). Hydrometeor contents retrieved from reflectivity data can also be assimilated using

Corresponding author: Haiqin Chen, haiqin.chen@nju.edu.cn

Publisher's Note: This article was revised on 29 March 2024 to correct the affiliations of the first author.

DOI: 10.1175/MWR-D-23-0196.1

variational methods (Sun and Crook 1998; Wang et al. 2013). To minimize hydrometeor retrieval errors, some research integrates additional information, such as flash extent density data from geostationary satellites (Fierro et al. 2016, 2019; Wang et al. 2018; Hu et al. 2020), dual-polarization radar (Ding et al. 2022), and background hydrometeor fields (Chen et al. 2020, 2021).

Beyond analyzing hydrometeors from radar reflectivity, assimilating other model state variables derived from reflectivity data, such as temperature and moisture, is also an active area of research. Water vapor mixing ratio (q_v) in the model initial conditions has been found to have a greater impact on convective-scale NWP than the hydrometeor fields (Fabry and Sun 2010; Ge et al. 2013), as it influences the formation of clouds, precipitation patterns, and energy exchange within convection. If q_v is accurately represented in the initial conditions, a more reasonable physical balance can be achieved in the analysis, sustaining the positive impact of radar data assimilation (DA). Given the physical importance of moisture modification over hydrometeor modification, numerous studies have focused on assimilating humidity information retrieved from reflectivity data.

Caumont et al. (2010) introduced a 1D+3DVar method that converts reflectivity into profiles of relative humidity using Bayesian theory. This approach has been successfully applied to models such as Météo-France's AROME model (Wattrelot et al. 2014), and the Japan Meteorological Agency's JNoVA system (Ikuta and Honda 2011). Wang et al. (2013) transformed reflectivity into q_v by assuming saturation within convection, and implemented this method in the WRFDA system, which has been incorporated into an operational system at the Beijing Urban Research Institute. Lai et al. (2019) utilized the vertically integrated liquid (VIL; Greene and Clark 1972) to retrieve humidity, resulting in more consistent reflectivity and updraft helicity forecasts for two tornado events when compared to the experiments without using VIL. In reality, the relationship between reflectivity and q_v is complex, and inferring q_v solely using radar reflectivity observations introduces substantial uncertainty. Our ongoing research aims to incorporate additional information, such as dual-polarization radar observations, to address these challenges.

After decades of research and development, radar polarimetry is quite mature. The U.S. operational WSR-88D network has been upgraded to dual-polarization (Kumjian 2013a), and other countries have also deployed or are in the process of upgrading their radar networks to dual-polarization (Zhang et al. 2019). Compared to conventional weather radar, dual-polarization weather radars transmit and receive electromagnetic waves in both horizontal and vertical orientations (polarization). Consequently, they can provide more comprehensive information about hydrometeor scatterers, including particle size, shape, and orientation (Bringi and Chandrasekar 2001) through the combined use of radar variables such as horizontal reflectivity (Z), differential reflectivity (Z_{DR}), specific differential phase (K_{DP}), and correlation coefficient (ρ_{hv}).

Dual-polarization radar has been leveraged for numerous applications, including severe weather detection, hydrometeor classification, quantitative precipitation estimation, and DA (see Zhang et al. 2019 for a review). For dual-polarization radar DA, substantial progress has been made on improving the hydrometeor initial field (Li and Mecikalski 2010, 2012; Posselt et al. 2015; Li et al. 2017; Kawabata et al. 2018; Zhang et al. 2021; Du et al. 2021). However, as previously mentioned, the benefits of assimilating hydrometeors alone may diminish rapidly, particularly in the 3DVar method; assimilating q_v information inferred from dual-polarization radar data may have a larger and sustained impact and warrants exploration (Caumont et al. 2010).

Augros et al. (2018) extended the Bayesian approach to incorporate dual-polarization radar data and found that the addition of K_{DP} resulted in a more plausible humidity analysis field. This adjustment had a slightly positive effect on convective-scale precipitation forecasting. Z_{DR} columns are commonly observed within or on the periphery of updrafts in deep moist convection. These updrafts lift supercooled raindrops and wet ice particles, leading to the occurrence of large Z_{DR} values above the 0°C isotherm (Kumjian 2013b; Kumjian et al. 2014; Snyder et al. 2015; Evaristo et al. 2022). Building upon the relationship between Z_{DR} columns and deep moist convection updrafts, Carlin et al. (2017), henceforth referred to as CJ17, used a modified complex cloud analysis to adjust q_v and latent heating within convection where Z_{DR} columns were detected. The study demonstrated that incorporating Z_{DR} column observations into the cloud analysis system improved the analysis and prediction of convection. However, CJ17 employed only a single dual-polarization radar for each case examined. Furthermore, the assimilation of Z_{DR} columns was performed using the cloud analysis method, which does not adequately account for background errors and observation errors in the DA process.

In this study, pseudo-q_v observations are retrieved based on Z_{DR} columns identified through a mosaic of data from multiple radar sites. These observations are then assimilated using the 3DVar framework with the aim of assessing the impact of these retrievals on convective-scale DA and forecasting. Section 2 provides an introduction to the 3DVar method, Z_{DR} column detection, and the q_v retrieval scheme. The model configuration and experimental setup are detailed in section 3. Section 4 describes the sensitivity experiments conducted on a squall-line case to optimize the assimilation of pseudo-q_v observations from Z_{DR} columns. The quantitative evaluation of four severe cases is presented in section 5. Finally, section 6 offers a summary and discussion.

2. Methodology

a. *The 3DVar system*

In this study, a 3DVar system that was initially developed by the Center for Analysis and Prediction of Storms (CAPS; Gao et al. 1999, 2004; Hu et al. 2006a,b; Ge et al. 2010) specifically for convective-scale radar DA is employed. This system was further refined at the National Severe Storms Laboratory (NSSL; Gao and Stensrud 2012; Gao et al. 2013; Hu et al. 2021). The optimal solution of the 3DVar is obtained by minimizing a cost function that quantifies the discrepancy between the observations and background valid at the analysis time:

TABLE 1. Summary of the criteria for Z_{DR} column detection.

Variable	Criteria
T	$-20° \le T \le 0°C$
Z	The max composite reflectivity within a neighborhood 3×3 grid box is above 30 dBZ
ρ_{hv}	$\rho_{hv} \ge 0.85$
Z_{DR}	More than two continuous levels observed Z_{DR} between 1.0 and 5.0 dB with vertical continuity; the bottom level is within 300 m of the 0°C level

$$J(\mathbf{x}) = \frac{1}{2}(\mathbf{x} - \mathbf{x}_b)^{\mathrm{T}}\mathbf{B}^{-1}(\mathbf{x} - \mathbf{x}_b) + \frac{1}{2}\{\mathbf{y} - H(\mathbf{x})\}^{\mathrm{T}}\mathbf{R}^{-1}\{\mathbf{y} - H(\mathbf{x})\} + J_c(\mathbf{x}), \quad (1)$$

where the vectors $\mathbf{x}$, $\mathbf{x}_b$, and $\mathbf{y}$ represent the analysis state, background state, and observations, respectively; H denotes the nonlinear observation operator, which transforms $\mathbf{x}$ into its equivalent in the observation space; $\mathbf{B}$ and $\mathbf{R}$ stand for the background error covariance and observation error covariance matrices, respectively; and J_c is a regularization term that allows the imposition of any weak constraint, resulting in a more balanced analysis.

Due to its relatively lower computational cost and demonstrated benefits (Chen et al. 2021), the indirect assimilation method is chosen in this study. In the indirect method, hydrometeors and q_v are first retrieved from reflectivity and the dual-polarization variables. Subsequently, these retrieved pseudo-observations are incorporated into the cost function represented by the second term on the rhs of Eq. (1):

$$J(q_h) = \frac{1}{2}(q_h - q_h^o)^{\mathrm{T}}\mathbf{R}_{q_h}^{-1}(q_h - q_h^o), \quad (2)$$

$$J(q_v) = \frac{1}{2}(q_v - q_v^o)^{\mathrm{T}}\mathbf{R}_{q_v}^{-1}(q_v - q_v^o), \quad (3)$$

where q_h and q_v denote the analysis of hydrometeor mixing ratios (rainwater, snow, and graupel) and water vapor mixing ratio, respectively; the superscript "o" signifies the corresponding pseudo-observations; and $\mathbf{R}_{q_h}$ and $\mathbf{R}_{q_v}$ represent the observation error covariances for hydrometeors and q_v, respectively. The technique for retrieving hydrometeors and q_v is described in section 2c.

b. Z_{DR} column detection

Dual-polarization radar data from the Next Generation Weather Radar (NEXRAD) network undergo quality control before being mapped to the model space, following the same procedure as described in CJ17. Subsequently, dual-polarization data from multiple radar sites are merged, producing three-dimensional mosaicked dual-polarization observations Z, Z_{DR}, K_{DP}, and ρ_{hv}. During the merging, reflectivity is set as the highest value from all radars, and the grid with the highest reflectivity value is chosen for the corresponding Z_{DR}, K_{DP}, and ρ_{hv} values.

Following Snyder et al. (2015) and CJ17, several criteria are established to ascertain whether a horizontal model grid point observes a Z_{DR} column (summarized in Table 1):

1) Areas of interest are confined to regions where the environmental temperature is between −20° and 0°C. This temperature constraint is used as Z_{DR} columns extend from the 0°C isotherm toward colder temperatures, and to help isolate the impact of high Z_{DR} from other sources, such as pristine ice crystals at cloud top.
2) ρ_{hv} is required to be above 0.85 to ensure a meteorological signal is detected.
3) Within a 3×3 grid box centered on a grid point, the maximum value of composite reflectivity should exceed 30 dBZ. The criterion employed in this study is more stringent than that in CJ17 to minimize the chance of false detection, which could lead to predictions of spurious convection.
4) The observed Z_{DR} must fall between 1 and 5 dB for more than two vertically adjacent grid boxes above the environmental 0°C level. The 5-dB threshold is set to limit the influence of pristine ice particles, which can contribute to large Z_{DR} values (Hogan et al. 2002). Additionally, the bottom of the Z_{DR} column should be situated within 300 m above the freezing level (0°C).

Following CJ17, a horizontal mode filter of 3 km × 3 km is applied to mitigate false detections. If at least five of the grids within the 3×3 area meet the aforementioned criteria, that grid is counted as a Z_{DR} column. The two-dimensional Z_{DR} column depth in model space is then used for the q_v retrieval.

c. Pseudo-hydrometeor and water vapor observations

Pseudo-hydrometeors, including rainwater, snow, and graupel mixing ratios, are retrieved from Z data using a background-dependent hydrometeor retrieval scheme (Chen et al. 2020). This scheme integrates background microphysical information to diagnose the contributions of each hydrometeor species to the total reflectivity.

The humidity control variable of the 3DVar system is q_v. Therefore, we choose to retrieve pseudo-q_v observations from the Z_{DR} columns. If a Z_{DR} column is observed, and its depth exceeds two model levels, saturation is assumed within

TABLE 2. Summary of four selected cases in May 2019.

Event date	SPC outlook category	No. of tornados, hail reports	Primary states affected	Primary storm mode
17 May	Enhanced	46, 76	CO, NE, KS, OK, WY, SD	Supercell
20 May	High	28, 69	OK, TX, AR, KS, MO	Mixed
22 May	Moderate	43, 42	OK, TX, MO, KS, IL, IA	Supercell
28 May	Moderate	26, 79	OK, MO, NE, KS, AR, IL, IA	Supercell

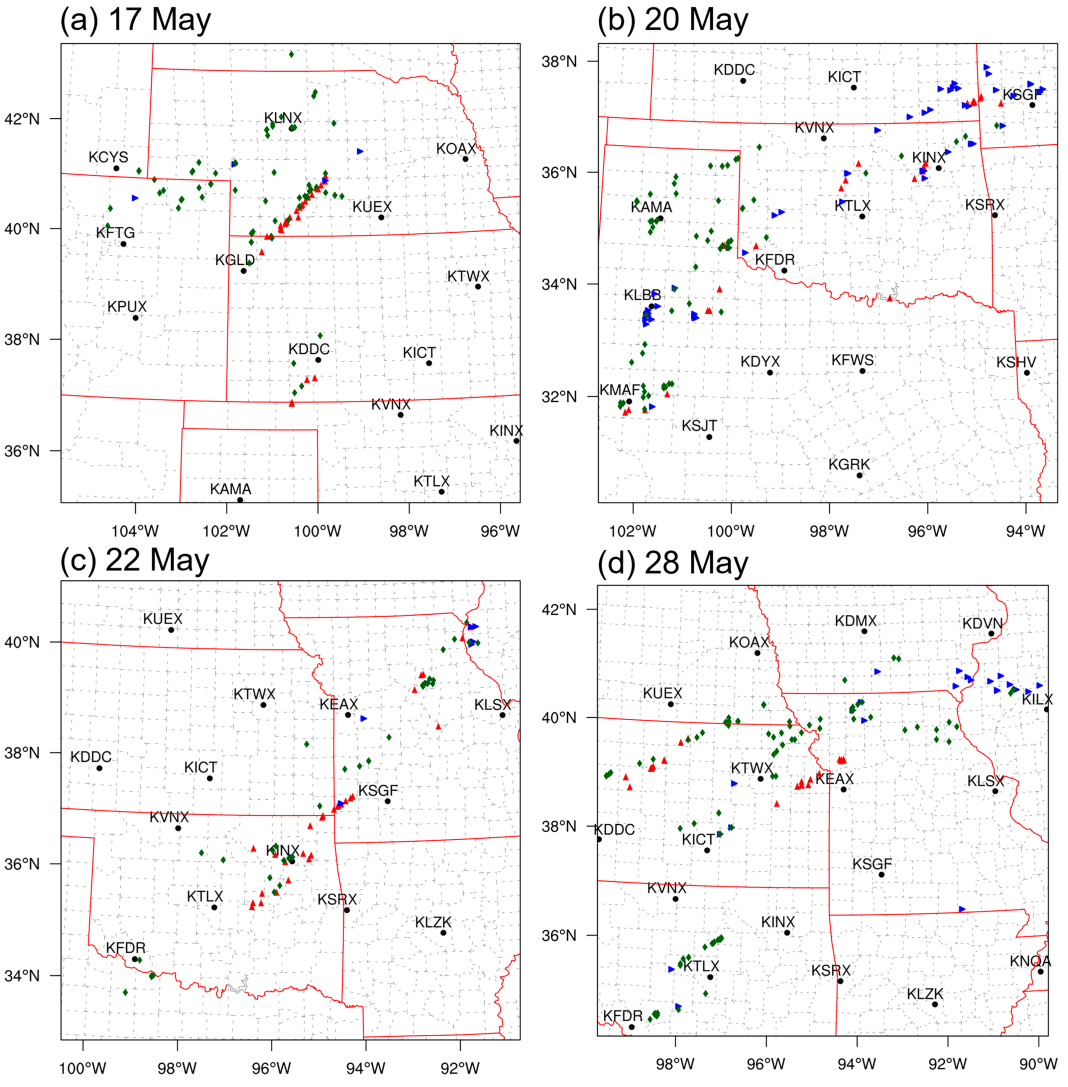

FIG. 1. The simulation domain, radar sites, and Storm Prediction Center (SPC) storm reports for (a) 17 May, (b) 20 May, (c) 22 May, and (d) 28 May 2019. The red triangles, green rhombuses, and blue triangles represent reports of tornados, hail, and damaging winds, respectively. NEXRAD sites' locations and names are marked with black dots and text labels.

the corresponding model column between the lifted condensation level (LCL) and a "cloud top" height defined by a reflectivity threshold of 18.5 dBZ (following Fierro et al. 2016; Lai et al. 2019). Given that the 3DVar method can propagate the observations in the model space using the background error covariance (BEC) decorrelation scale, we have opted not to directly adjust the q_v field surrounding the Z_{DR} column in the retrieval process, as was done by CJ17 for the cloud analysis approach. Furthermore, the Z_{DR} column-based q_v suppression and temperature adjustment scheme in CJ17 are not implemented in this study due to the absence of significant positive impact. Instead, we employ a neighborhood no-rain reflectivity assimilation approach (Gao et al. 2018) to mitigate spurious convection. Under this approach, if the background reflectivity surpasses 30 dBZ, yet reflectivity below 0 dBZ is observed in over 75% of the surrounding grid points (within a 30 km × 30 km × 6-level area), pseudo-q_v observations are scaled down to 90% of the background specific humidity at that grid point.

3. Experimental design

a. *Four chosen severe weather events*

In this study, four severe weather events occurring in May 2019 have been selected as the testing cases: 17, 20, 22, and 28 May. A summary of these cases is provided in Table 2, which includes the dates, the Storm Prediction Center (SPC) severe weather risk levels, SPC tornado and hail report counts, as well as the storm mode for each of the four cases. First, the 20 May squall-line event is studied in detail to

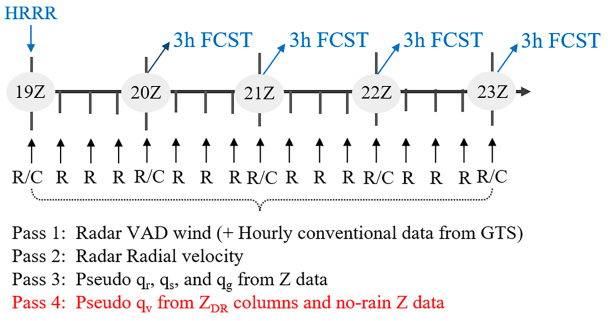

FIG. 2. Schematic diagram depicting the 15-min rapid DA and forecasting experiments. Observations include conventional observations (denoted as "C") and radar-related observations (denoted as "R"), including radar VAD wind, radial velocity, hydrometeor retrievals from Z, and q_v retrievals from Z_{DR} columns. Various observations are assimilated in separate passes, with the option of including pass 4 contingent upon the experimental design.

evaluate the impact of assimilating q_v retrievals from Z_{DR} columns on the analyses and subsequent forecasts. Through a series of sensitivity experiments, an optimal assimilation configuration is identified. Subsequently, this configuration is applied to the four cases and a quantitative evaluation is carried out to provide an objective assessment.

b. Model configuration

The NWP model used in this study is the Advanced Research Weather and Forecasting (ARW-WRF) model V3.8.1 (Skamarock and Klemp 2008). The experimental configurations for the four cases are nearly identical, differing primarily in the chosen domain, which is determined by the locations of the severe weather events. Figure 1 presents the simulation domains for the four cases, along with reports of damaging winds, hail, and tornadoes. The horizontal grid spacing is set at 1.5 km, employing a grid of 601 × 601 cells. The model consists of 51 stretched vertical levels, with the model top positioned at 50 hPa. In line with the real-time settings of the Warn-on-Forecast (WoF) system (Jones et al. 2018; Wang et al. 2019), the selected physical parameterizations include the Thompson microphysical scheme (Thompson et al. 2008), Rapid Radiative Transfer Model for General circulation models (RRTMG) long-wave and short-wave radiation schemes (Iacono et al. 2008), and the Yonsei University planetary boundary layer (PBL) physics scheme (Hong et al. 2004). No cumulus scheme is employed.

c. Experimental design

To assess the effects of assimilating pseudo-q_v observations from Z_{DR} columns, several 15-min rapid cycling DA and forecasting experiments are conducted, following the schematic diagram depicted in Fig. 2. All experiments are initialized at 1900 UTC, with the initial and boundary conditions derived from the High-Resolution Rapid Refresh (HRRR) model forecast product (Smith et al. 2008). DA procedures are executed from 1900 to 2300 UTC, with a frequency of every 15 min. Except for the first cycle, the background fields are determined by the 15-min forecast from the preceding DA cycle. A 3-h forecast is launched every hour from 2000 to 2300 UTC.

A multiple-pass procedure, as described by Gao et al. (2013), is employed for assimilating the multisource and multiscale observations. In the first pass, conventional observations from the Global Telecommunication System (GTS) and Doppler radar Vertical Azimuth Display (VAD) winds are assimilated using a horizontal BEC decorrelation scale of 60 km. In the second pass, radial velocity is assimilated with a 12-km decorrelation scale. In the third pass, retrievals of rainwater, snow, and graupel mixing ratios from Z data are assimilated with a 6-km decorrelation scale. In the final pass, pseudo-q_v observations obtained from both Z_{DR} columns and no-rain Z data are assimilated. Notably, VAD winds, radial velocity, and hydrometeor retrievals from Z data are assimilated at 15-min intervals, while conventional observations are assimilated hourly. Following Chen et al. (2021), the pseudo-hydrometeor observation errors are set to 0.1 g kg^{-1}. The assimilated NEXRAD site locations for each case are shown in Fig. 1.

To explore the optimal configuration for assimilating pseudo-q_v observations from Z_{DR} columns, a series of sensitivity experiments are undertaken. These experiments include tests for observation error, decorrelation scale, and assimilation frequency. The benchmark, labeled Exp-CNTL, serves as the control experiment without Z_{DR} assimilation. The other experiments incorporate pseudo-q_v observations under various configurations.

The assessment of pseudo-q_v observation error sensitivity begins by comparing three experiments, Exp-ZDR, Exp-ZDR-Err1p0, and Exp-ZDR-Err2p0, which use q_v observation errors

TABLE 3. Summary of assimilation configurations used for all experiments.

Experiment	Observation error for pseudo-q_v (g kg^{-1})	Horizontal length scale (km)	Z_{DR} columns assimilation frequency (min)
Exp-CNTL	No water vapor retrievals are assimilated		
Exp-ZDR	0.5	6	15
Exp-ZDR-Err1p0	1.0	6	15
Exp-ZDR-Err2p0	2.0	6	15
Exp-ZDR-Len12	0.5	12	15
Exp-ZDR-Len18	0.5	18	15
Exp-ZDR-30m	0.5	6	30
Exp-ZDR-60m	0.5	6	60

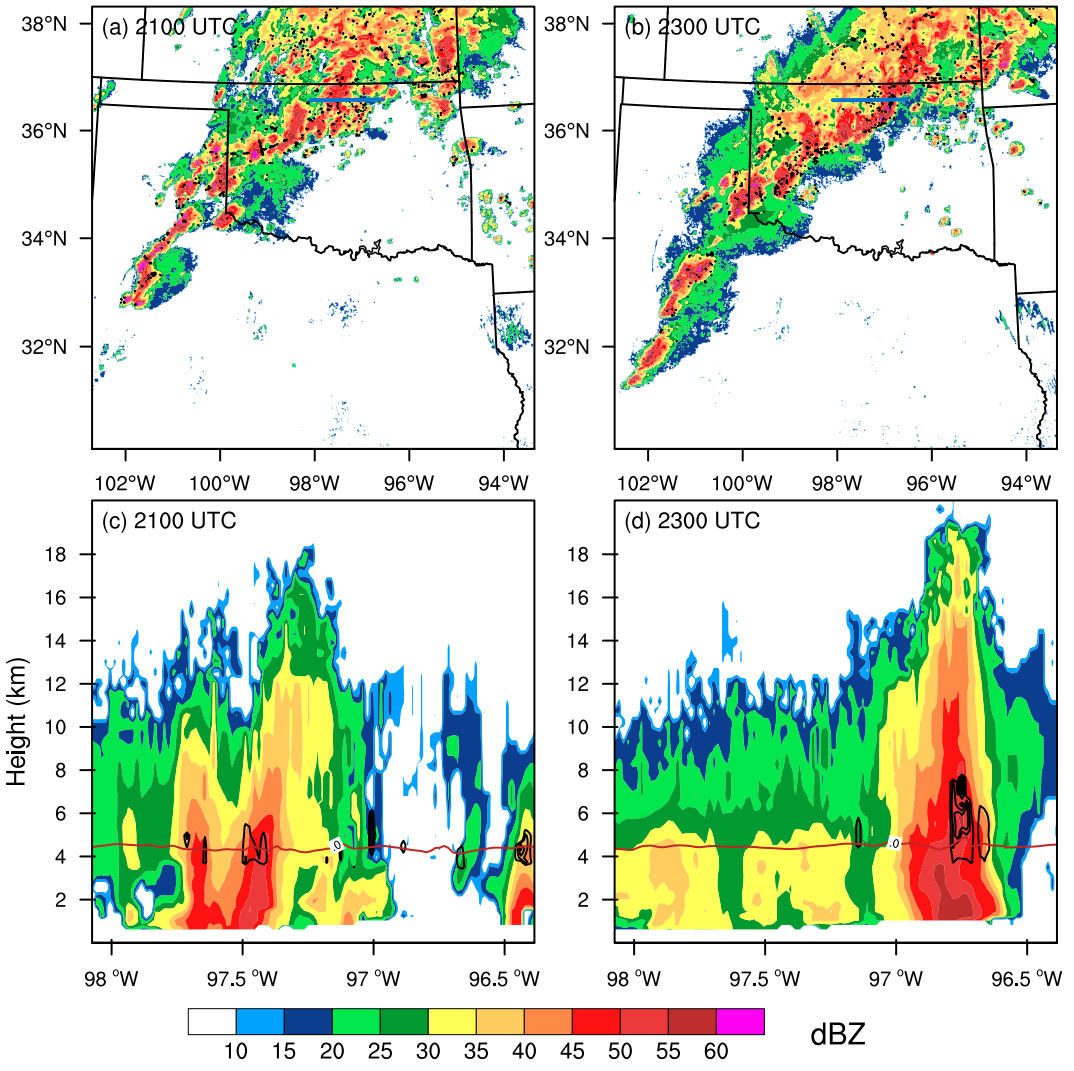

FIG. 3. Z_{DR} column identification indicated by observed reflectivity (shaded; dBZ) and Z_{DR} (contoured; 1 dB) at 2 km AGL at (a) 2100 and (b) 2300 UTC, accompanied by a vertical cross section at (c) 2100 and (d) 2300 UTC along the blue line marked in (a) and (b). The red lines in (c) and (d) denote the 0°C level.

of 0.5, 1.0, and 2.0 g kg^{-1}, respectively. The evaluation of different BEC decorrelation scales (6, 12, and 18 km) is carried out through the comparison between Exp-ZDR, Exp-ZDR-Len12, and Exp-ZDR-Len18. Another set of sensitivity experiments aims to gauge the influence of diverse assimilation frequencies for pseudo-q_v observations from Z_{DR} columns. Specifically, assimilation frequencies of 15, 30, and 60 min are utilized for Exp-ZDR, Exp-ZDR-30m, and Exp-ZDR-60m, respectively. Table 3 provides an overview of the assimilation configurations adopted in these experiments.

4. Case study on 20 May 2019

This section focuses on assessing the influence of assimilating q_v retrievals from Z_{DR} columns in the context of a squall-line case on 20 May 2019. First, the impact of Z_{DR} column assimilation on the analysis field is examined by identifying Z_{DR} columns and analyzing q_v increments. Subsequently, three distinct sets of sensitivity experiments are conducted to determine the optimal assimilation configurations. These configurations include variations in observation errors, horizontal decorrelation scale, and assimilation frequency of the q_v retrievals.

a. *Identification of Z_{DR} columns and water vapor increments*

Figures 3a and 3b displays the positions of identified Z_{DR} columns superimposed on the composite reflectivity at 2100 and 2300 UTC. At 2100 UTC, robust convection spanning Kansas, Oklahoma, and Texas is beginning to merge into a line. The majority of Z_{DR} columns are situated within the high-reflectivity zone, while a few isolated columns emerge in areas characterized by relatively weaker reflectivity. The presence of Z_{DR} columns signifies many updrafts in the system, aligning with the high reflectivity areas (above 45 dBZ). By

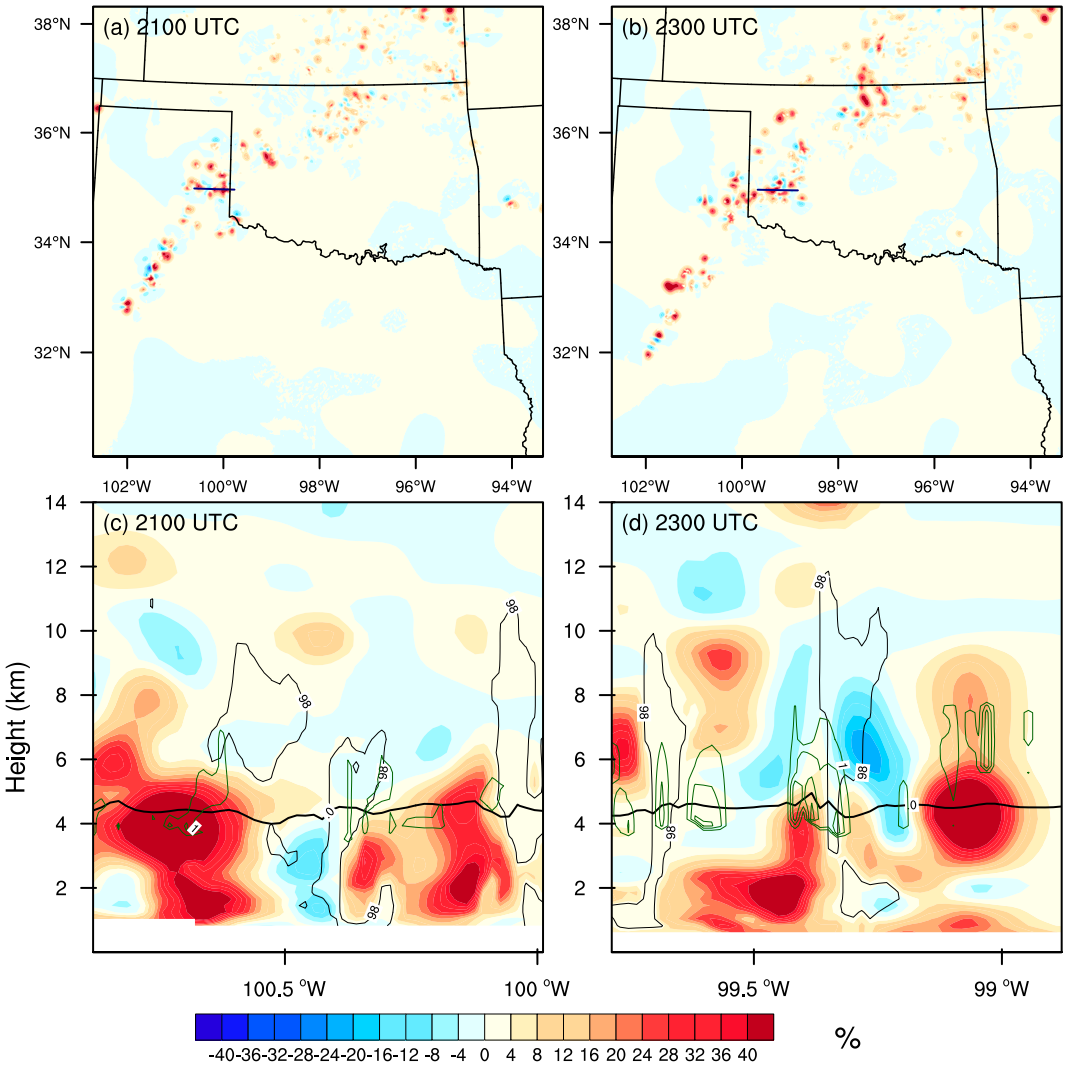

FIG. 4. Analysis increments of relative humidity (shaded; %) and Z_{DR} (green contours; 1 dB) at the tenth model level at (a) 2100 and (b) 2300 UTC, accompanied by a vertical cross section at (c) 2100 and (d) 2300 UTC along the black line in (a) and (b). The blue lines in (c) and (d) indicate the 0°C level. Additionally, the black contour in (c) and (d) represents a relative humidity of 98%.

2300 UTC (Fig. 3b), a mature squall line exists with a break in the line around 100.5°W. The intensity and extent of strong echoes in the northern sector continues to escalate, while reflectivity in the southwest portion of the domain also intensifies, impacting central Texas. A high density of Z_{DR} columns predominantly appear at the leading edge of the squall line, correlating with high precipitation areas, and the isolated Z_{DR} columns are comparatively reduced, implying enhanced system organization. Vertical cross-sections depicting the Z_{DR} values along the blue lines are illustrated in Figs. 3c and 3d. At 2100 UTC, the Z_{DR} columns are situated within the convection cores, characterized by relatively shallow depths, indicative of existing updrafts and ongoing cell development. By 2300 UTC, the Z_{DR} columns emerge on the inflow side of the storm cell, displaying greater depth, indicative of a more mature stage for the convective cell.

Figure 4 illustrates the analysis increments of relative humidity at 2100 and 2300 UTC in Exp-ZDR. Focusing on the tenth vertical level (around 2.5 km AGL) (Figs. 4a,b), there is a noticeable enhancement of humidity fields within the regions where Z_{DR} columns are detected. Notably, larger increments are observed in Texas and Oklahoma compared to Kansas. At 2300 UTC, the presence of high-density Z_{DR} columns leads to more substantial and concentrated increments in q_v. However, the no-rain assimilation scheme does introduce some negative humidity increments in regions where the background convection exhibits displacement errors. Examining the vertical cross-section of relative humidity increments along 35°N in Figs. 4c and 4d, it is evident that the moisture increases in areas coinciding with Z_{DR} columns. Moreover, these increments in higher levels are more pronounced at 2300 UTC, aligning with the mature stage of the developing

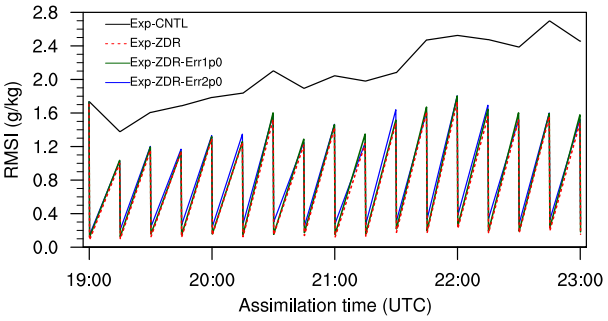

FIG. 5. RMSIs of forecast (higher values in the sawtooth-shaped curves) and analysis (lower values) for q_v (g kg^{-1}) during 4-h assimilation cycles of Exp-CNTL, Exp-ZDR, Exp-ZDR-Err1p0, and Exp-ZDR-Err2p0.

squall-line system. These humidity increments collectively highlight that the assimilation of Z_{DR} columns serves to enhance q_v analysis within the convection.

b. *Sensitivity of observation errors*

The 3DVar method offers distinct advantages over cloud analysis by incorporating background information into the analysis through background and observation error covariances. This subsection is dedicated to exploring the sensitivity of the DA and forecast to pseudo-q_v observation errors. For Exp-ZDR, Exp-ZDR-Err1p0, and Exp-ZDR-Err2p0, the observation errors are set to 0.5, 1.0, and 2.0 g kg^{-1}, respectively.

To evaluate the performance of the 3DVar system in assimilating q_v retrievals from the Z_{DR} columns, we first calculate the root-mean-square innovations (RMSI) of both the analysis and forecasts of q_v during the DA cycles for Exp-CNTL, Exp-ZDR, Exp-ZDR-Err1p0, and Exp-ZDR-Err2p0. The RMSI metric serves to quantify the evolution of the innovations, which denotes the discrepancy between the observations (here the pseudo-q_v) and the model states modified by assimilation. The RMSIs are computed within the region where the pseudo-q_v observations exceed 1.0 g kg^{-1}. Exp-CNTL demonstrates the highest RMSIs, and these values rise in tandem with the evolution of the squall-line system (Fig. 5). Notably, while RMSIs for the forecast and analysis in all three Z_{DR} experiments exhibit a zigzag pattern across cycles, the incorporation of pseudo-q_v observations from Z_{DR} columns results in significantly smaller RMSIs compared to Exp-CNTL. It is evident that the analysis from three Z_{DR} experiments closely aligns with the pseudo-q_v observations. This alignment between the analysis and observations also results in lower RMSIs for the forecasts, proving the stable performance of the pseudo-q_v assimilation.

Utilizing the RMSIs for both the forecasts and analyses, we recalculate the observation error for pseudo-q_v from Z_{DR} columns using the method proposed by Desroziers et al. (2005), which is calculated by the statistical expectation of the cross-product between $O - A$ (here O denotes observation, A denotes analysis) difference and the $O - B$ (B denotes background) difference. This recalculation yields an estimated observation error of 0.635, 0.502, and 0.500 g kg^{-1} using the samples from Exp-ZDR-Err2p0, Exp-ZDR-Err1p0 and Exp-ZDR, respectively, with the latter two very close to the 0.5 g kg^{-1} employed in Exp-ZDR. Therefore, we opted to keep the observation error for pseudo-q_v observations from Z_{DR} columns for three other real data cases in this study at 0.5 g kg^{-1}.

Figure 6 depicts the fractions skill scores (FSS; Roberts and Lean 2008) for the 0–3-h composite reflectivity forecasts during the assimilation cycles from 2000 to 2300 UTC, utilizing an neighborhood radius of 12 km. For the 20-dBZ threshold (Fig. 6a), all three Z_{DR} experiments exhibit similar FSS values, consistently outperforming the Exp-CNTL without Z_{DR} assimilation. At the 40-dBZ threshold, the three Z_{DR} experiments are

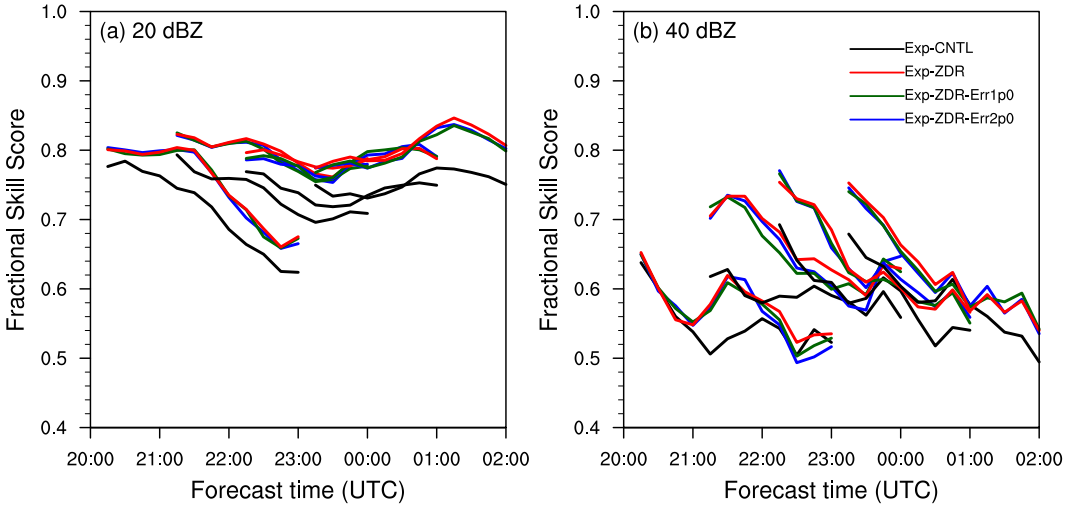

FIG. 6. Fractional skill scores of 0–3-h composite reflectivity forecasts for (a) 20- and (b) 40-dBZ thresholds over the entire forecast cycles for Exp-CNTL, Exp-ZDR, Exp-ZDR-Err1p0, and Exp-ZDR-Err2p0. The output frequency is 15 min. The neighborhood radius is set to 12 km.

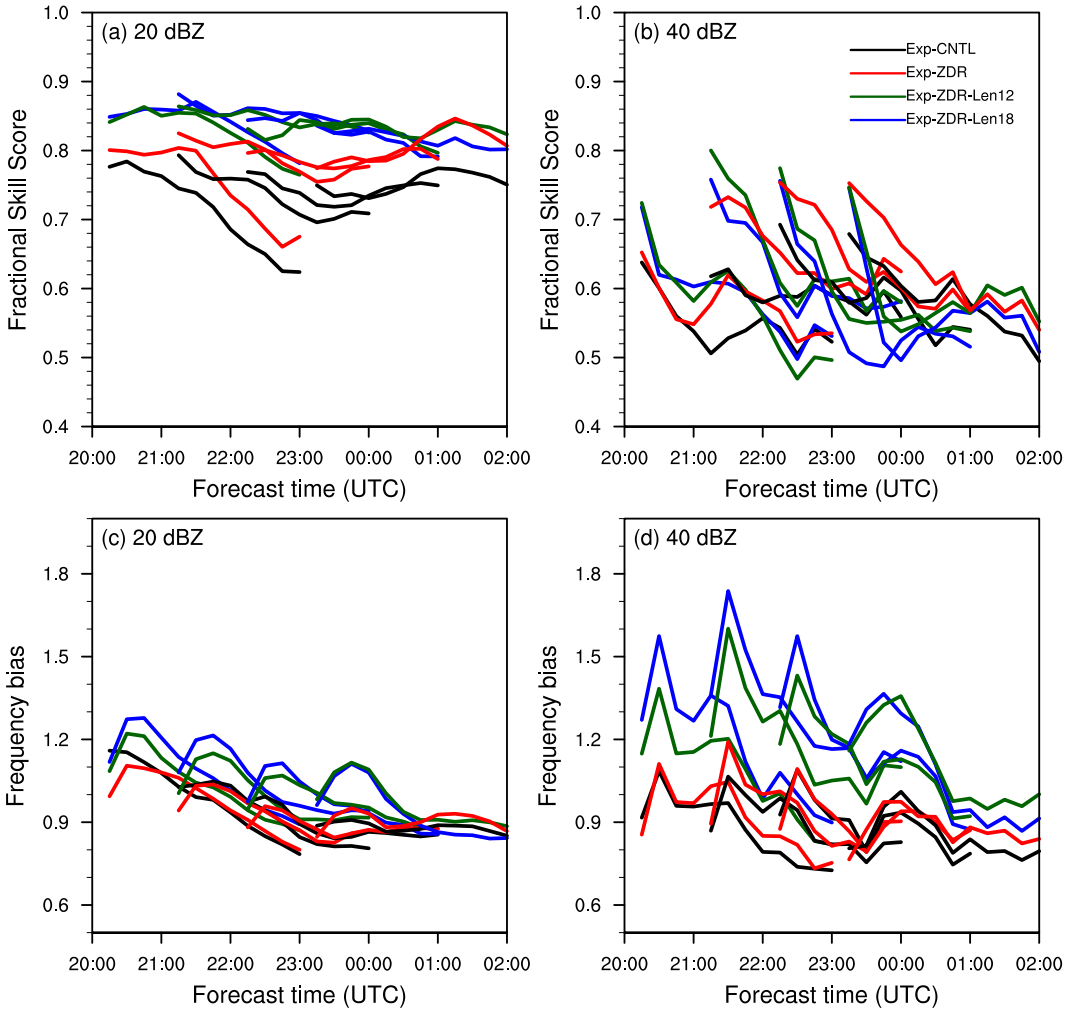

FIG. 7. (a),(b) Fractional skill scores and (c),(d) frequency bias of 0–3-h composite reflectivity forecasts for (a),(c) 20- and (b),(d) 40-dBZ thresholds over the entire forecast cycles for Exp-CNTL, Exp-ZDR, Exp-ZDR-Len12, and Exp-ZDR-Len18. The output frequency is 15 min. The neighborhood radius of FSSs used is 12 km.

consistently better than Exp-CNTL. Notably, Exp-ZDR demonstrates slightly higher FSS values across most cycles compared to Exp-ZDR-Err1p0 and Exp-ZDR-Err2p0, implying that a smaller observation error for the pseudo-q_v observations would yield greater benefits for Z_{DR} column assimilation.

c. *Sensitivity to horizontal decorrelation scale*

In CJ17, the adjustment of q_v in surrounding columns was directly based on the depth of the Z_{DR} columns. The 3DVar method has the capacity to distribute observations in the model space through spatial correlations, which are defined by the decorrelation scale in the BEC. As a result, we investigate the effects of different horizontal decorrelation scales on the assimilation of pseudo-q_v observations from Z_{DR} columns and its subsequent impact on forecasts. In these experiments, we set the horizontal decorrelation scales to 6, 12, and 18 km for Exp-ZDR, Exp-ZDR-Len12, and Exp-ZDR-Len18, respectively, while maintaining a fixed vertical decorrelation scale of 2 km. Although the vertical decorrelation scale's impact was also tested, it was found to be less sensitive compared to the horizontal scale, so those results are not presented in this study.

Figure 7 shows FSSs and frequency bias for the 0–3-h composite reflectivity forecasts across four assimilation cycles spanning from 2000 to 2300 UTC for Exp-CNTL, Exp-ZDR, Exp-ZDR-Len12, and Exp-ZDR-Len18. The assimilation of q_v derived from Z_{DR} columns is notably sensitive to the horizontal decorrelation scale. For the lower 20-dBZ threshold, larger horizontal length scales result in higher FSS values at an expense of overestimation in Exp-ZDR-Len12 and Exp-ZDR-Len18. However, at the 40-dBZ threshold, Exp-ZDR demonstrates higher FSS values and frequency bias closer to 1 compared to Exp-ZDR-Len12 and Exp-ZDR-Len18, with Exp-ZDR's superiority steadily increasing with the assimilation cycles, while the FSS of the Exp-ZDR-Len12 and Exp-ZDR-Len18 even drops to below Exp-CNTL due to

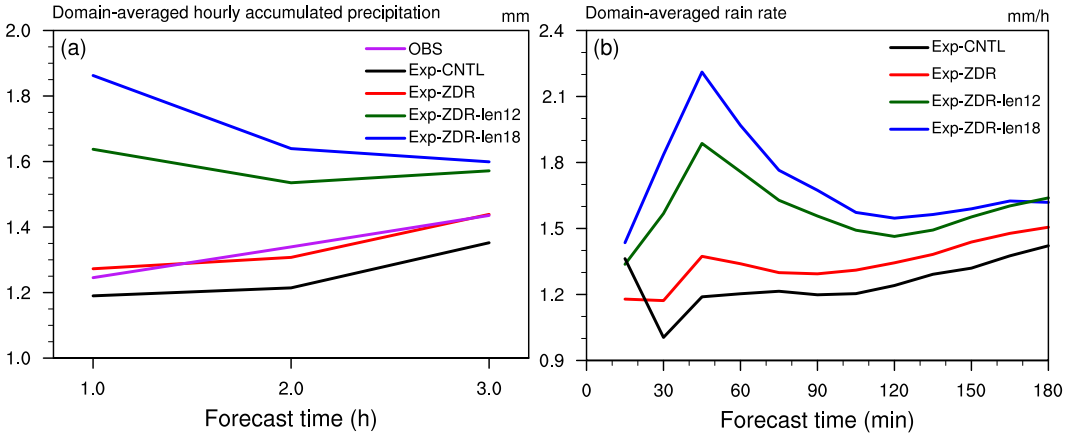

FIG. 8. (a) Hourly accumulated precipitation (mm) averaged over four cycles from 2000 to 2300 UTC from four experiments and the corresponding NCEP's Stage-IV products. (b) Rain rate (mm h^{-1}) averaged over four cycles for the 180-min forecast period for Exp-CNTL, Exp-ZDR, Exp-ZDR-len12, and Exp-ZDR-len18.

the overestimation, indicated by their much larger high-frequency bias scores.

To find the reason behind the decrease in forecast skill for high reflectivity regions when employing longer decorrelation scales, we compare the hourly accumulated precipitation against the NCEP's Stage-IV product and the temporal evolution of domain-averaged rain rate for the four experiments. These values are averaged over four DA cycles spanning from 2000 to 2300 UTC, and the results are presented in Fig. 8.

It is quite remarkable that Exp-ZDR closely aligns with the observed precipitation, while Exp-CNTL underestimates the precipitation, and both Exp-ZDR-Len12 and Exp-ZDR-Len18 overestimate it (Fig. 8a). In the case of Exp-CNTL, there is a noticeable reduction in precipitation rate during the first 15–30-min integration period (Fig. 8b). This phenomenon can be attributed to the added hydrometeors, which quickly fall out and cannot be sustained without appropriate humidity conditions. Thanks to the assimilation of Z_{DR} columns, this sharp reduction in precipitation rate is not observed in the other three experiments (Fig. 8b). However, both Exp-ZDR-Len12 and Exp-ZDR-Len18 exhibit an initial surge in precipitation rate during the first hour, followed by a gradual decline. This behavior arises due to the larger decorrelation scale spreading the q_v increments over a wider region. Consequently, excessive humidity accumulates, leading to a rapid increase in precipitation rate and a subsequent overprediction of total rainfall. In comparison, Exp-ZDR maintains a stable precipitation rate throughout the entire 3-h forecast. This stability suggests that a decorrelation scale of 6 km is optimal for assimilating pseudo-q_v observations from Z_{DR} columns, as it ensures an accurate and well-balanced representation of the moisture fields.

d. Sensitivity to the assimilation frequency

In this subsection, we investigate the sensitivity of the DA and forecast to the assimilation frequency of pseudo-q_v observations derived from Z_{DR} columns. Specifically, we consider assimilation frequencies of 15, 30, and 60 min for Exp-ZDR, Exp-ZDR-30m, and Exp-ZDR-60m, respectively.

Figure 9 illustrates the 1–3-h composite reflectivity forecasts initialized at 2300 UTC (the final assimilation cycle) for Exp-CNTL and the three Z_{DR} sensitivity experiments. In the 1-h forecast Exp-CNTL accurately predicts the squall-line system in the north of Oklahoma (system A in Fig. 9a), while the three Z_{DR} experiments exhibit a western bias (comparing the first column of Fig. 9). However, Exp-CNTL incurs substantial location errors for the northern cells in Texas (system B), which are gradually mitigated with increasing assimilation frequency of q_v retrievals from Z_{DR} columns. As for the 2-h forecast, all four experiments predict a similar squall-line system in Oklahoma. Notably, the assimilation of Z_{DR} columns leads to reduced location errors and heightened convective cell intensities in Texas, especially for system B (Figs. 9h,k,n). This trend continues in the 3-h forecast (Figs. 9i,l,o), where Exp-CNTL presents a distinct eastern bias in the convection of system B, spanning from the center of Oklahoma to the northern part of Texas (Fig. 9f). Furthermore, increasing the assimilation frequency of pseudo-q_v observations from Z_{DR} columns results in improved forecast accuracy, particularly in terms of reducing location errors and enhancing the representation of convective systems in the forecasted squall line.

Figure 10 provides the temporal evolution of the fractions skill scores (FSS) for 0–3-h composite reflectivity forecasts against the composite reflectivity observation, throughout four assimilation cycles spanning 2000–2300 UTC 20 May. For the 20-dBZ threshold, all three Z_{DR} experiments consistently outperform Exp-CNTL with superior FSS values. Notably, Exp-ZDR, the experiment with highest assimilation frequency of pseudo-q_v observations has the largest FSS values. For the 40-dBZ threshold, the observed trend remains consistent with the 20-dBZ results. The benefits of Exp-ZDR are more prominently displayed and remain stable across the assimilation cycles. These results affirm that the assimilation of pseudo-q_v observations from Z_{DR} columns positively

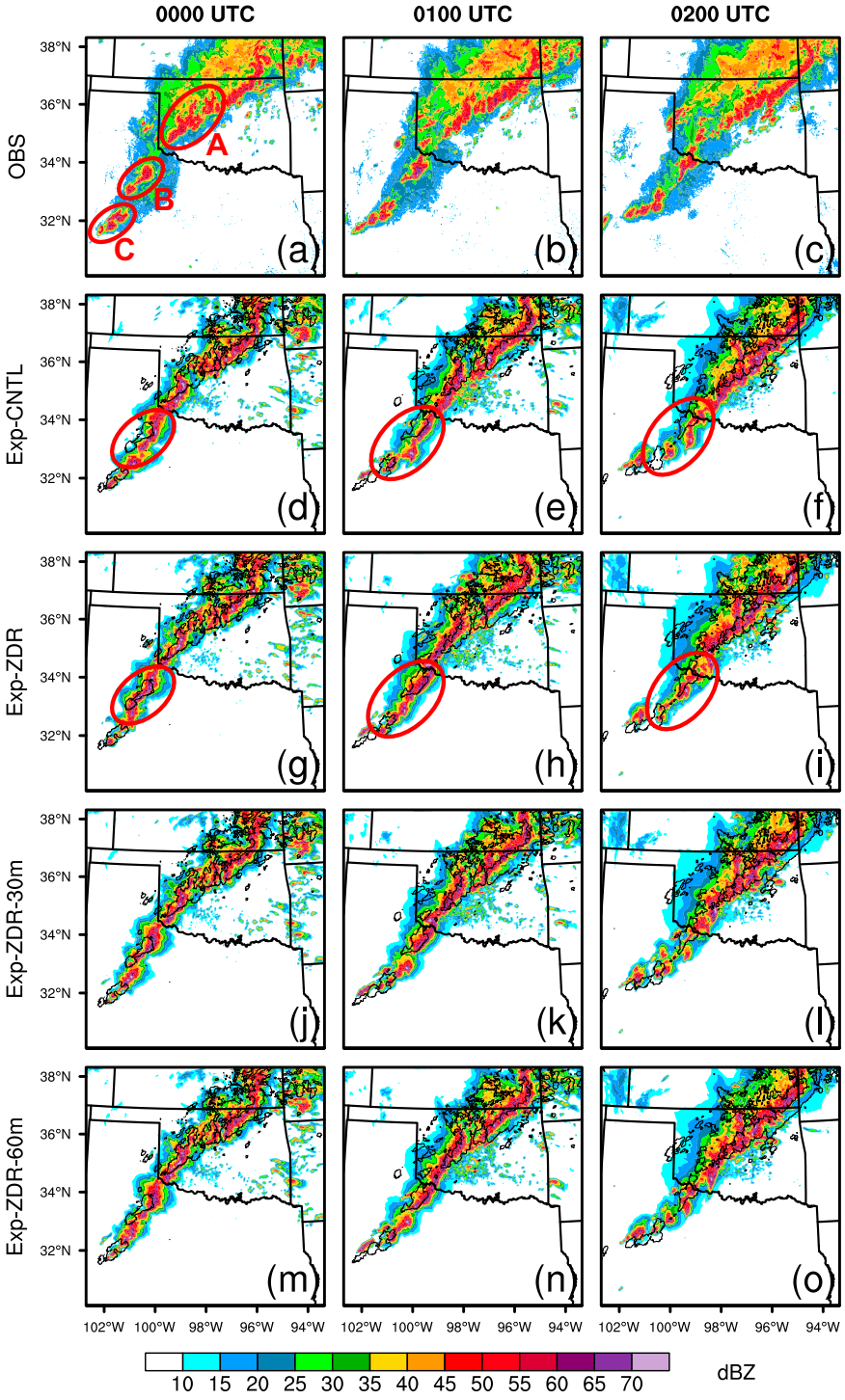

FIG. 9. (a)–(c) Observed composite reflectivity, and the corresponding 1–3-h forecasts initialized from 2300 UTC 20 May 2019 in (d)–(f) Exp-CNTL, (g)–(i) Exp-ZDR, (j)–(l) Exp-ZDR-30m, and (m)–(o) Exp-ZDR-60m at (left) 0000, (center) 0100, and (right) 0200 UTC, respectively. The black contours indicate the observed composite reflectivity of 40 dBZ. For the reader's convenience, we have distinguished the three different clusters labeled as A, B, and C and the differences between Exp-CNTL and Exp-ZDR are highlighted in red circles.

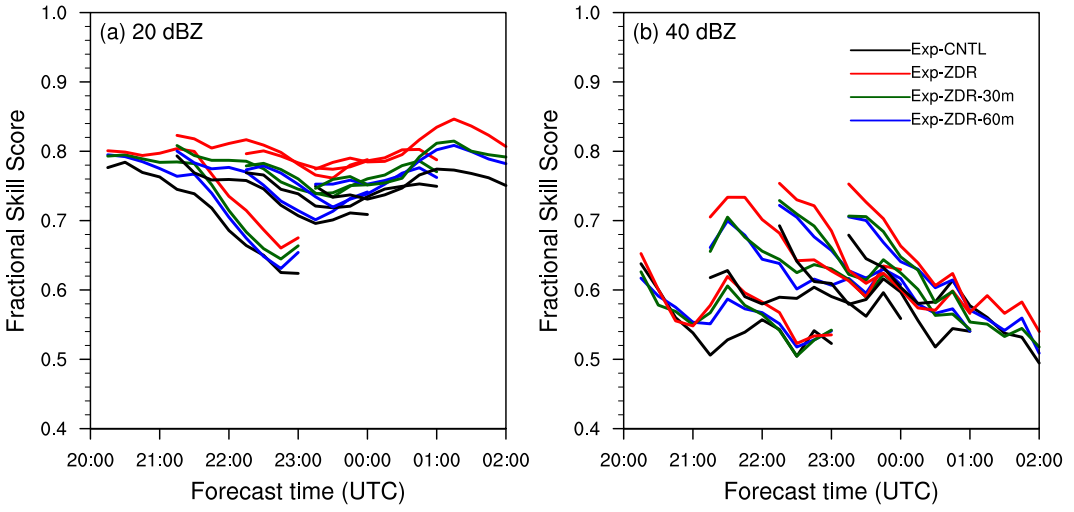

FIG. 10. Fractional skill scores of 0–3-h composite reflectivity forecasts for (a) 20- and (b) 40-dBZ thresholds over the entire forecast cycles for Exp-CNTL, Exp-ZDR, Exp-ZDR-30m, and Exp-ZDR-60m. The neighborhood radius is 12 km.

contributes to the forecast accuracy, particularly when a higher DA frequency is employed.

Figure 11 provides a closer look at the impact of high-frequency assimilation of Z_{DR} columns on short-term predictions, focusing on the precipitable water vapor (PWV) analysis at 2000 and 2300 UTC. At 2000 UTC, Exp-ZDR exhibits elevated PWV values over Oklahoma and Texas, regions closely associated with severe weather occurrences (Fig. 11b). By 2300 UTC, the cumulative effect of cycling assimilation becomes more evident, with noticeable disparities between the four experiments. Relative to Exp-CNTL, the assimilation of pseudo-q_v observations from Z_{DR} columns results in greater PWV analysis within the Oklahoma squall-line system and Texas supercells (Figs. 11f–h). This enhancement becomes even more pronounced with the 15-min assimilation frequency employed in Exp-ZDR (Fig. 11f). Elevated PWV levels in these

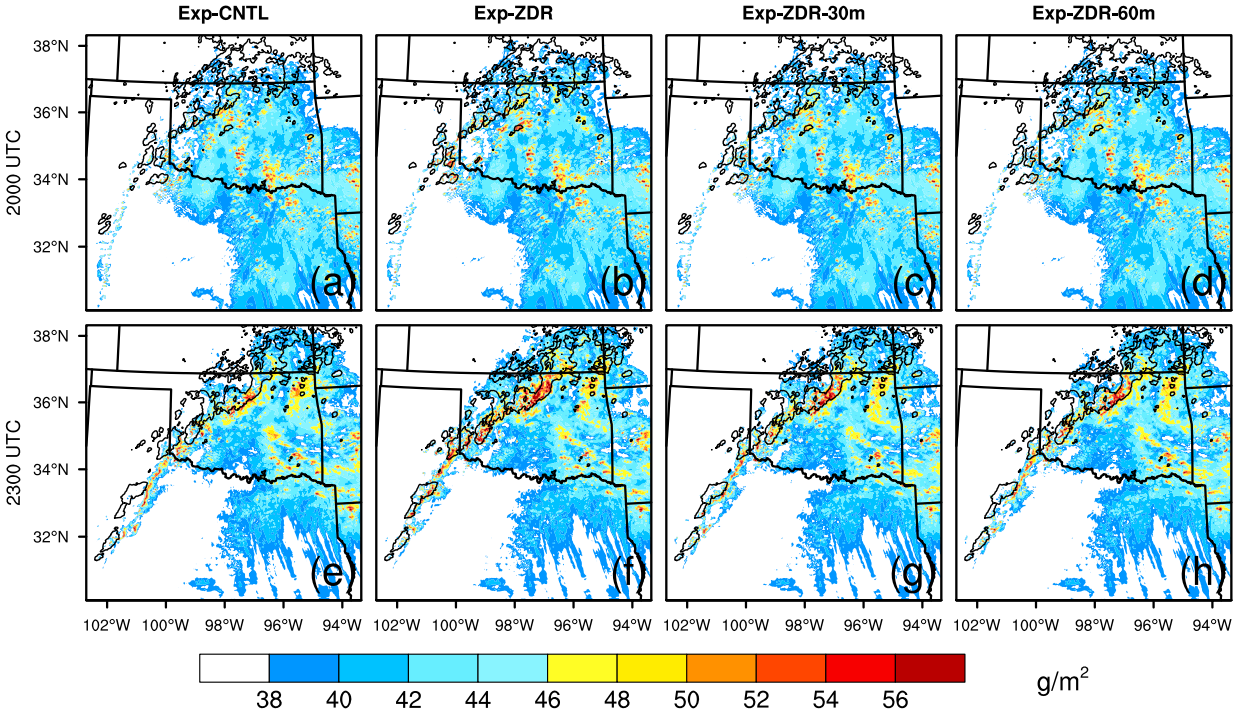

FIG. 11. Precipitable water vapor (shaded; g m^{-2}) at (a)–(d) 2000 and (e)–(h) 2300 UTC for (a),(e) Exp-CNTL; (b),(f) Exp-ZDR; (c),(g) Exp-ZDR-30m; and (e),(h) Exp-ZDR-60m. The black contours indicate the observed composite reflectivity of 40 dBZ.

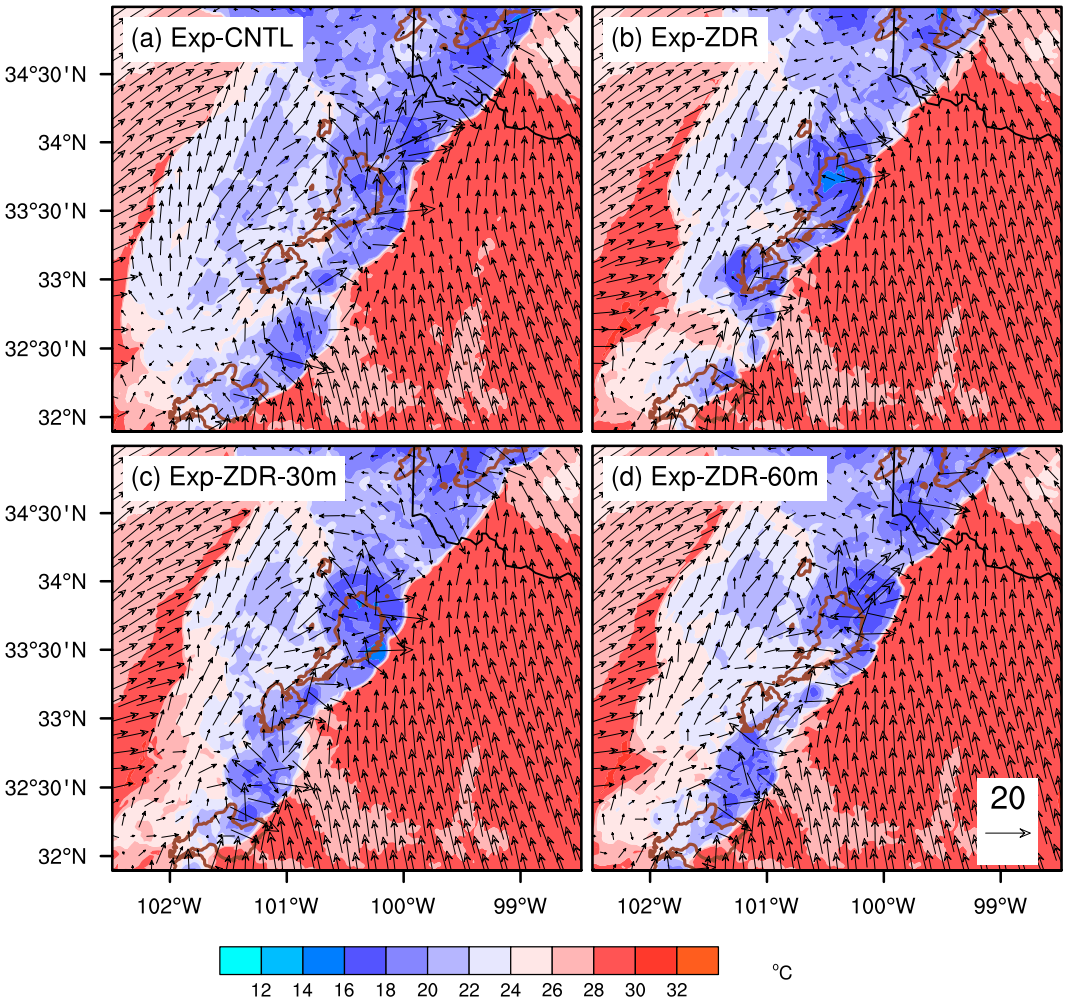

FIG. 12. 1-h forecasts of surface temperature (shaded; °C) and winds (vectors; m s^{-1}) initialized from 2300 UTC 20 May 2019. The brown contour indicates the observed composite reflectivity of 45 dB*Z*.

convective regions are expected to contribute to improved forecast accuracy for accumulated precipitation, especially for heavy rainfall.

Figure 12 offers insights into the impact of cycling assimilation of Z_{DR} columns on 1-h forecasts of surface winds and temperature for the final assimilation cycle across the four experiments. The fast-moving storms generate descending airflow behind the leading edge of these storms, which reaches the surface and leads to the formation of cold pools. All experiments predict cold pools and diverging winds near the convections in Texas. However, Exp-CNTL exhibits a weaker cold pool intensity near the central convections and shows obvious displacement errors. This situation gets improved when q_v retrievals from Z_{DR} columns are assimilated. With an increase in assimilation frequency, the intensity of wind gusts and cold pools gradually rises, leading to a corresponding reduction in displacement errors. In general, the 15-min cycling assimilation of pseudo-q_v observations from Z_{DR} columns bolsters the convection by providing stronger surface-level cold pools and wind divergence. This, in turn, contributes to the improved short-term forecasting of convective cells.

5. Multiple case evaluation

In this section, the study progresses with the quantitative evaluation of four severe weather cases. The optimal configuration determined from the sensitivity experiments, which focused on observation error, decorrelation scale, and assimilation frequency for q_v retrievals from Z_{DR} columns with the squall-line case on 20 May 2019, is employed to gauge the enhanced predictive capabilities brought about by the assimilation of pseudo-q_v observations from Z_{DR} columns in short-term severe weather forecasts. This comprehensive evaluation aims to further ascertain the added value of Z_{DR} column assimilation in improving the accuracy of forecasts for severe weather events.

Figure 13 provides insights into the predictive performance through categorical performance diagrams (Roebber 2009) for the four severe weather cases. These diagrams incorporate

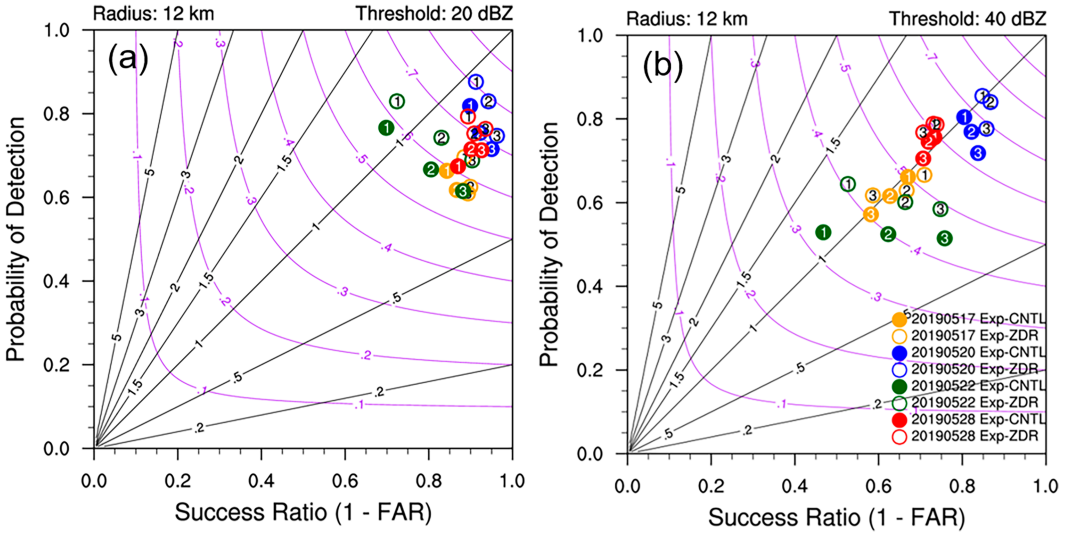

FIG. 13. Performance diagrams for composite reflectivity forecasts for each case at thresholds of (a) 20 and (b) 40 dBZ with a neighborhood radius of 12 km. Black and purple lines represent constant BIAS and CSI, respectively. Digits on the dots indicate the hour into the forecast.

various metrics such as probability of detection (POD), critical success index (CSI), frequency bias (BIAS), and success ratio (SR) to evaluate forecast accuracy. For the 20-dBZ threshold, assimilating Z_{DR} columns contributes to substantial enhancements in the 22 and 20 May cases, manifesting as increased POD and CSI. Although the improvements are slightly more moderate for the other two cases, Exp-ZDR consistently demonstrates superior forecast skills compared to Exp-CNTL. Furthermore, the magnitude of the biases, shown as ratios on the diagonal lines of Fig. 13, are notably reduced in Exp-ZDR, moving it closer to an ideal value of 1. For the 40-dBZ threshold, Exp-ZDR consistently surpasses Exp-CNTL across all four cases, exhibiting higher POD, CSI, and improved BIAS alignment with the optimal value of 1. This affirms the positive impact of assimilating pseudo-q_v observations from Z_{DR} columns on the short-term composite reflectivity forecasts over a 0–3-h period.

Figure 14 provides a consolidated view of the averaged FSS and frequency bias for reflectivity forecasts across the four severe weather cases, including the entire 3-h forecast period, evaluated for both the 20- and 40-dBZ thresholds. For the 20-dBZ threshold, Exp-ZDR substantially outperforms Exp-CNTL, exemplified by noticeably higher FSSs and closer frequency bias to 1.0 for the entire duration of forecasts. This indicates that the inclusion of Z_{DR} column assimilation contributes to a more accurate forecast of composite reflectivity over time. For the 40-dBZ threshold, Exp-ZDR also shows a performance advantage over Exp-CNTL over the entirety of the 3-h forecast period. While the gap in performance between Exp-ZDR and Exp-CNTL narrows with leading time, Exp-ZDR consistently maintains higher FSSs and larger frequency bias scores despite slight overestimation. This underscores that assimilating pseudo-q_v observations from Z_{DR} columns leads to improved forecasts regarding the intensity of convection.

In Fig. 15, the case-averaged FSSs and frequency bias for the hourly accumulated precipitation forecasts are depicted, comparing Exp-CNTL and Exp-ZDR against Stage-IV precipitation data. Over the 3-h forecast window, Exp-ZDR consistently displays higher FSS values than Exp-CNTL for various precipitation thresholds (1, 2.5, and 5 mm), reflecting improvements in the occurrence and spatial distribution of light to moderate precipitation. For the 10-mm threshold, Exp-ZDR attains higher FSS values than Exp-CNTL in the 1- and 2-h forecasts, accompanied by an acceptable level of overestimation. In essence, assimilating pseudo-q_v observations from Z_{DR} columns positively impacts the accuracy of short-term precipitation forecasts.

6. Conclusions

The Z_{DR} column, a distinctive polarimetric radar signature, serves as a valuable indicator of updrafts in deep moist convection. In this study, pseudo-q_v observations are obtained by assuming that the q_v field between LCL and cloud top is saturated within the detected Z_{DR} column region. These retrievals are subsequently assimilated using the 3DVar method, which provides initial conditions for the convective-scale WRF model. The effects of assimilating Z_{DR} columns are initially assessed through a case study involving a squall-line event on 20 May 2019. The optimal assimilation configuration is determined through a series of sensitivity experiments. Furthermore, experiments for four severe weather cases in May 2019 are conducted to comprehensively evaluate the impact of assimilating pseudo-q_v observations from Z_{DR} columns on short-term severe weather forecasting.

The analysis of the 20 May 2019 squall-line case reveals that Z_{DR} columns appear in the mature regions of convective systems, with some also observed in developing convection. Sensitivity experiments are conducted to evaluate the impact

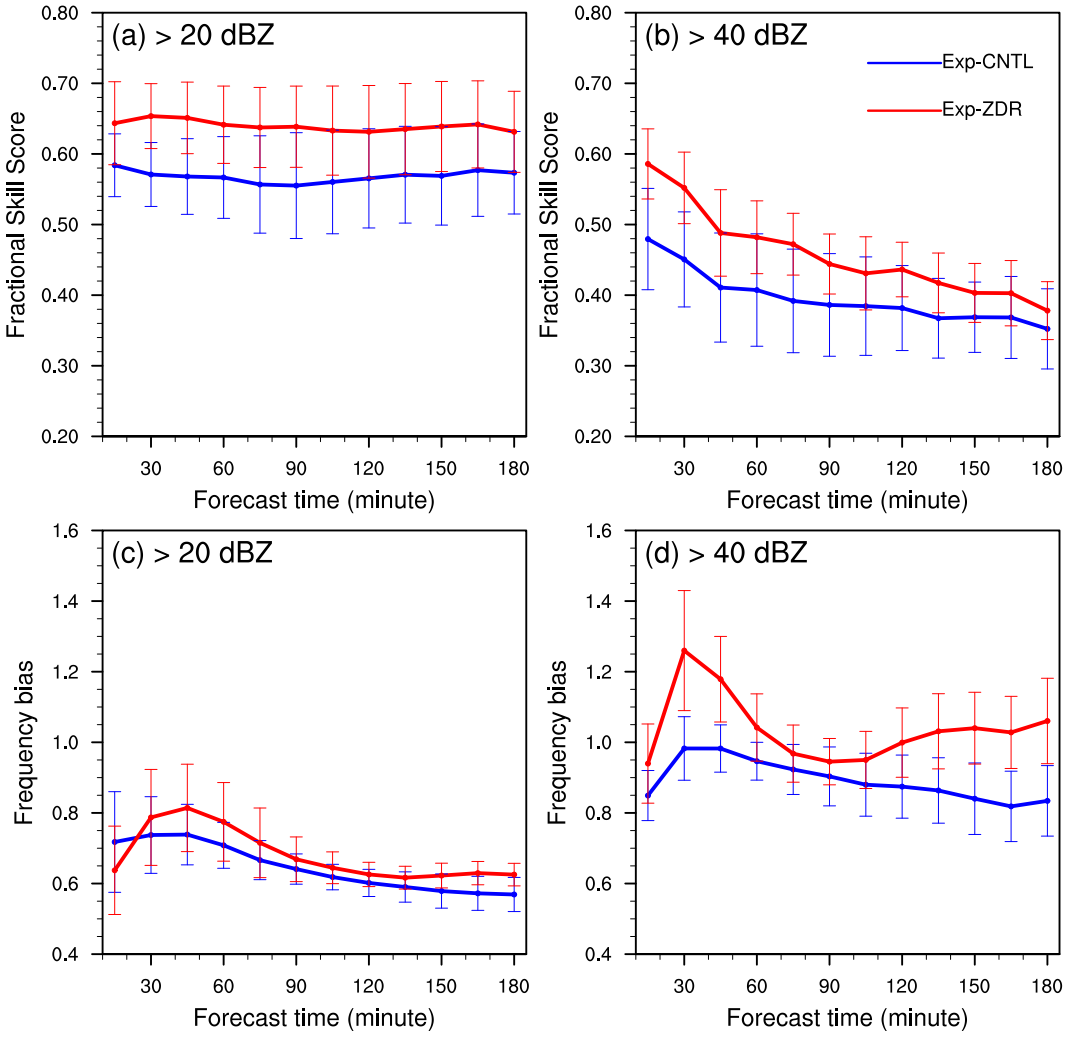

FIG. 14. Fractional skill scores and frequency bias of 0–3-h composite reflectivity forecasts for (a),(c) 20- and (b),(d) 40-dBZ thresholds averaged over the entire forecast cycles of four cases. Error bars represent the 95% confidence intervals. The output frequency is 15 min. The neighborhood radius of FSSs is 12 km.

of different factors on the assimilation of pseudo-q_v observations from Z_{DR} columns.

1) Observation errors sensitivity: The experiments indicate that short-term forecasts are not highly sensitive to observation errors. Nevertheless, the smaller observation error (0.5 g kg^{-1}) lead to a better analysis and forecast of this squall-line case.
2) Horizontal decorrelation scale sensitivity: The experiments reveal that a relatively shorter horizontal decorrelation scale (6 km) yields higher forecast skill. Larger decorrelation scales (12 and 18 km) lead to rapid increases in predicted rain rates during the first hour of the forecast, resulting in overestimated precipitation and decreased forecast skill.
3) Assimilation frequency sensitivity: The experiments demonstrate that frequent assimilation (15-min cycling) of pseudo-q_v observations produces stable improvements in both reflectivity and precipitation forecasts. The high-frequency assimilation enhances the precipitable q_v within convective regions and strengthens cold pools and surface divergent winds, creating more favorable conditions for convection.

Overall, these sensitivity experiments underscore the value of assimilating pseudo-q_v observations from Z_{DR} columns, highlighting the need for accurate observation errors, optimal horizontal decorrelation scales, and high assimilation frequencies to maximize the positive impact on short-term forecasts of severe weather events.

The quantitative evaluation of four severe weather cases in May 2019 using the optimal assimilation configuration derived from the sensitivity experiments provides valuable insights into the impact of assimilating pseudo-q_v observations from Z_{DR} columns. Performance diagrams and FSSs illustrate that assimilating pseudo-q_v observations from Z_{DR} columns helps enhance the accuracy and skill of the forecasting system, ultimately leading to improved severe weather predictions.

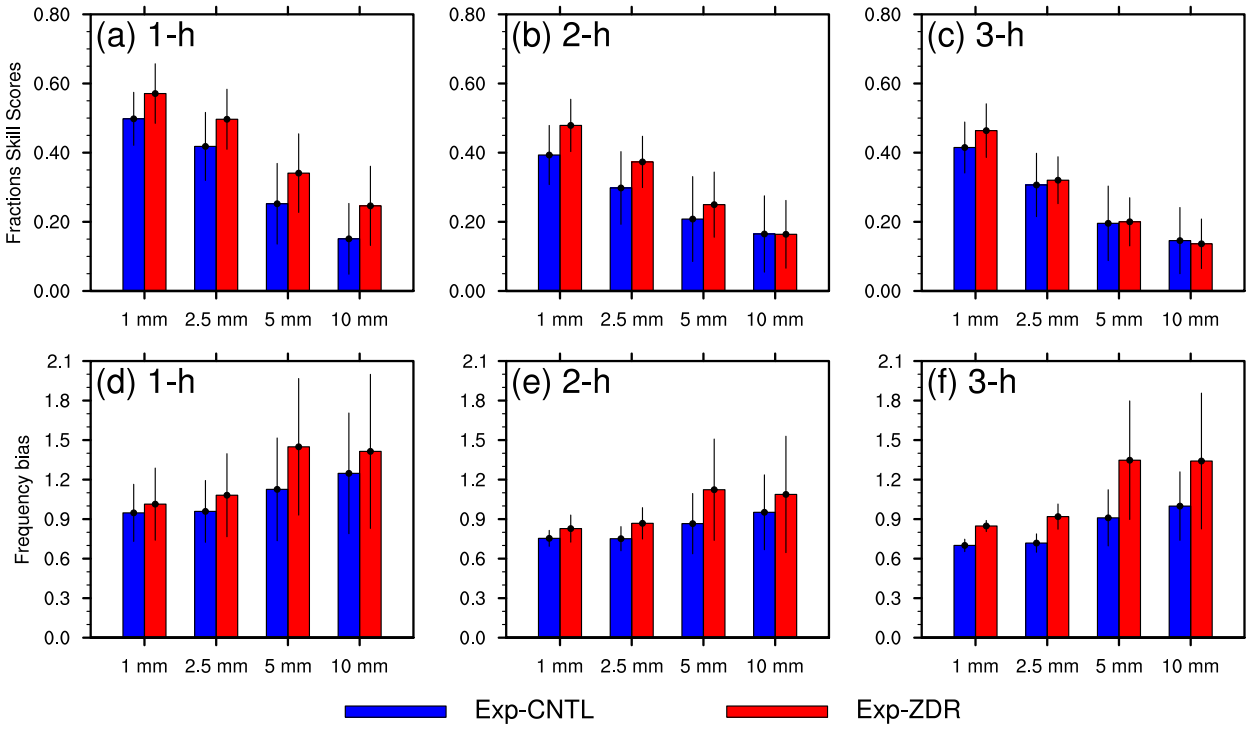

FIG. 15. Case-averaged (a)–(c) fractional skill scores and (d)–(f) frequency bias of hourly accumulated precipitation forecasts against NCEP Stage-IV observations for thresholds of 1.0, 2.5, 5, and 10 mm for the (a),(d) 1-; (b),(e) 2-; and (c),(f) 3-h forecasts. Error bars represent the 95% confidence intervals. The neighborhood radius of FSSs is 12 km.

Even though promising results are obtained, the assimilation of pseudo-q_v observations from Z_{DR} columns should be evaluated through more cases so that robust conclusions can be made. Expanding the assimilation approach to include other retrieved variables, such as temperature and vertical velocity derived from Z_{DR} columns, or other polarimetric signatures of updrafts, such as K_{DP} columns (e.g., van Lier-Walqui et al. 2016), may provide valuable avenues for future research. It would also be interesting to compare the direct assimilation of Z_{DR} with the indirect assimilation of the retrievals using the ensemble DA method. Besides, the use of a hybrid ensemble-variational method can provide a more balanced analysis by incorporating both ensemble-based and variational-based assimilation techniques. This could potentially address limitations of the climatology-based background error covariance and better capture the dynamics and flow-dependent relationships between variables. Finally, improved automated detection methods for Z_{DR} columns (e.g., Krause and Klaus 2023) will more easily facilitate their assimilation in the future. Overall, continued research and experimentation in this area will likely lead to advancements in our understanding of DA techniques and their applications in short-term severe weather forecasting.

Acknowledgments. This work was supported by the Open Grants of the State Key Laboratory of Severe Weather (Grant 2021LASW-A01), China Meteorological Administration Tornado Key Laboratory (Grant TKL202301), NOAA/Office of Oceanic and Atmospheric Research under NOAA–University of Oklahoma Cooperative Agreement NA21OAR4320204, U.S. Department of Commerce, and partially supported by U.S. National Science Foundation Grant AGS-2136161. Computing resources were provided by OU Supercomputing Center for Education and Research (OSCER).

Data availability statement. The Global Transmission System (GTS) conventional observations are obtained from NCAR's Research Data Archive (RDA) (https://rda.ucar.edu/datasets/ds351.0 and https://rda.ucar.edu/datasets/ds461.0). The HRRR analysis and forecast are obtained from the WoF Program. The NEXRAD Level II data can be downloaded using the AWS service (https://s3.amazonaws.com/noaa-nexrad-level2/index.html).

REFERENCES

Albers, S. C., J. A. McGinley, D. L. Birkenheuer, and J. R. Smart, 1996: The Local Analysis and Prediction System (LAPS): Analyses of clouds, precipitation, and temperature. *Wea. Forecasting*, **11**, 273–287, https://doi.org/10.1175/1520-0434(1996)011<0273:TLAAPS>2.0.CO;2.

Augros, C., O. Caumont, V. Ducrocq, and N. Gaussiat, 2018: Assimilation of radar dual-polarization observations in the AROME model. *Quart. J. Roy. Meteor. Soc.*, **144**, 1352–1368, https://doi.org/10.1002/qj.3269.

Benjamin, S. G., and Coauthors, 2004: An hourly assimilation–forecast cycle: The RUC. *Mon. Wea. Rev.*, **132**, 495–518,

https://doi.org/10.1175/1520-0493(2004)132<0495:AHACTR>2.0.CO;2.

Bringi, V. N., and V. Chandrasekar, 2001: *Polarimetric Doppler Weather Radar*. 1st ed. Cambridge University Press, 636 pp.

Carlin, J. T., J. Gao, J. C. Snyder, and A. V. Ryzhkov, 2017: Assimilation of Z_{DR} columns for improving the spinup and forecast of convective storms in storm-scale models: Proof-of-concept experiments. *Mon. Wea. Rev.*, **145**, 5033–5057, https://doi.org/10.1175/MWR-D-17-0103.1.

Caumont, O., V. Ducrocq, É. Wattrelot, G. Jaubert, and S. Pradier-Vabre, 2010: 1D+3Dvar assimilation of radar reflectivity data: A proof of concept. *Tellus*, **62A**, 173–187, https://doi.org/10.1111/j.1600-0870.2009.00430.x.

Chen, H., Y. Chen, J. Gao, T. Sun, and J. T. Carlin, 2020: A radar reflectivity data assimilation method based on background-dependent hydrometeor retrieval: An observing system simulation experiment. *Atmos. Res.*, **243**, 105022, https://doi.org/10.1016/j.atmosres.2020.105022.

——, J. Gao, Y. Wang, Y. Chen, T. Sun, J. Carlin, and Y. Zheng, 2021: Radar reflectivity data assimilation method based on background-dependent hydrometeor retrieval: Comparison with direct assimilation for real cases. *Quart. J. Roy. Meteor. Soc.*, **147**, 2409–2428, https://doi.org/10.1002/qj.4031.

Desroziers, G., L. Berre, B. Chapnik, and P. Poli, 2005: Diagnosis of observation, background and analysis-error statistics in observation space. *Quart. J. Roy. Meteor. Soc.*, **131**, 3385–3396, https://doi.org/10.1256/qj.05.108.

Ding, Z., K. Zhao, K. Zhu, Y. Feng, H. Huang, and Z. Yang, 2022: Assimilation of polarimetric radar observation with GSI cloud analysis for the prediction of a squall line. *Geophys. Res. Lett.*, **49**, e2022GL098253, https://doi.org/10.1029/2022GL098253.

Du, M., J. Gao, G. Zhang, Y. Wang, P. L. Heiselman, and C. Cui, 2021: Assimilation of polarimetric radar data in simulation of a supercell storm with a variational approach and the WRF model. *Remote Sens.*, **13**, 3060, https://doi.org/10.3390/rs13163060.

Evaristo, R., R. Reinoso-Rondinel, J.-Y. Chen, and S. Trömel, 2022: A synergetic approach to study differential reflectivity (ZDR) columns for precipitation. *11th European Conf. on Radar in Meteorology and Hydrology*, Locarno, Switzerland, ERAD, NCT.P7, https://www.erad2022.ch/_files/ugd/25a7b1_23b223c508be440ca402c5a29bba166e.pdf.

Fabry, F., and J. Sun, 2010: For how long should what data be assimilated for the mesoscale forecasting of convection and why? Part I: On the propagation of initial condition errors and their implications for data assimilation. *Mon. Wea. Rev.*, **138**, 242–255, https://doi.org/10.1175/2009MWR2883.1.

Fierro, A. O., J. Gao, C. L. Ziegler, K. M. Calhoun, E. R. Mansell, and D. R. MacGorman, 2016: Assimilation of flash extent data in the variational framework at convection-allowing scales: Proof-of-concept and evaluation for the short term forecast of the 24 May 2011 tornado outbreak. *Mon. Wea. Rev.*, **144**, 4373–4393, https://doi.org/10.1175/MWR-D-16-0053.1.

——, Y. Wang, J. Gao, and E. R. Mansell, 2019: Variational assimilation of radar data and GLM lightning-derived water vapor for the short-term forecasts of high-impact convective events. *Mon. Wea. Rev.*, **147**, 4045–4069, https://doi.org/10.1175/MWR-D-18-0421.1.

Gao, J., and D. J. Stensrud, 2012: Assimilation of reflectivity data in a convective-scale, cycled 3DVAR framework with hydrometeor classification. *J. Atmos. Sci.*, **69**, 1054–1065, https://doi.org/10.1175/JAS-D-11-0162.1.

——, M. Xue, A. Shapiro, and K. K. Droegemeier, 1999: A variational method for the analysis of three-dimensional wind fields from two Doppler radars. *Mon. Wea. Rev.*, **127**, 2128–2142, https://doi.org/10.1175/1520-0493(1999)127<2128:AVMFTA>2.0.CO;2.

——, ——, K. Brewster, and K. K. Droegemeier, 2004: A three-dimensional variational data analysis method with recursive filter for Doppler radars. *J. Atmos. Oceanic Technol.*, **21**, 457–469, https://doi.org/10.1175/1520-0426(2004)021<0457:ATVDAM>2.0.CO;2.

——, and Coauthors, 2013: A real-time weather-adaptive 3DVAR analysis system for severe weather detections and warnings. *Wea. Forecasting*, **28**, 727–745, https://doi.org/10.1175/WAF-D-12-00093.1.

Gao, S., J. Sun, J. Min, Y. Zhang, and Z. Ying, 2018: A scheme to assimilate "no rain" observations from Doppler radar. *Wea. Forecasting*, **33**, 71–88, https://doi.org/10.1175/WAF-D-17-0108.1.

Ge, G., J. Gao, K. Brewster, and M. Xue, 2010: Impacts of beam broadening and Earth curvature on storm-scale 3D variational data assimilation of radial velocity with two Doppler radars. *J. Atmos. Oceanic Technol.*, **27**, 617–636, https://doi.org/10.1175/2009JTECHA1359.1.

——, ——, and M. Xue, 2013: Impacts of assimilating measurements of different state variables with a simulated supercell storm and three-dimensional variational method. *Mon. Wea. Rev.*, **141**, 2759–2777, https://doi.org/10.1175/MWR-D-12-00193.1.

Greene, D. R., and R. A. Clark, 1972: Vertically integrated liquid water—A new analysis tool. *Mon. Wea. Rev.*, **100**, 548–552, https://doi.org/10.1175/1520-0493(1972)100<0548:VILWNA>2.3.CO;2.

Gustafsson, N., and Coauthors, 2018: Survey of data assimilation methods for convective-scale numerical weather prediction at operational centers. *Quart. J. Roy. Meteor. Soc.*, **144**, 1218–1256, https://doi.org/10.1002/qj.3179.

Hogan, R. J., P. R. Field, A. J. Illingworth, R. J. Cotton, and T. W. Choularton, 2002: Properties of embedded convection in warm-frontal mixed-phase cloud from aircraft and polarimetric radar. *Quart. J. Roy. Meteor. Soc.*, **128**, 451–476, https://doi.org/10.1256/003590002321042054.

Hong, S.-Y., J. Dudhia, and S.-H. Chen, 2004: A revised approach to ice microphysical processes for the bulk parameterization of clouds and precipitation. *Mon. Wea. Rev.*, **132**, 103–120, https://doi.org/10.1175/1520-0493(2004)132<0103:ARATIM>2.0.CO;2.

Hu, J., A. O. Fierro, Y. Wang, J. Gao, and E. R. Mansell, 2020: Exploring the assimilation of GLM-derived water vapor mass in a cycled 3DVAR framework for the short-term forecasts of high-impact convective events. *Mon. Wea. Rev.*, **148**, 1005–1028, https://doi.org/10.1175/MWR-D-19-0198.1.

——, and Coauthors, 2021: Evaluation of an experimental Warn-on-Forecast 3DVAR analysis and forecast system on quasi-real-time short-term forecasts of high impact weather events. *Quart. J. Roy. Meteor. Soc.*, **147**, 4063–4082, https://doi.org/10.1002/qj.4168.

Hu, M., M. Xue, and K. Brewster, 2006a: 3DVAR and cloud analysis with WSR-88D Level-II data for the prediction of the Fort Worth, Texas, tornadic thunderstorms. Part I: Cloud analysis and its impact. *Mon. Wea. Rev.*, **134**, 675–698, https://doi.org/10.1175/MWR3092.1.

——, ——, J. Gao, and K. Brewster, 2006b: 3DVAR and cloud analysis with WSR-88D level-II data for the prediction of the

Fort Worth, Texas, tornadic thunderstorms. Part II: Impact of radial velocity analysis via 3DVAR. *Mon. Wea. Rev.*, **134**, 699–721, https://doi.org/10.1175/MWR3093.1.

Iacono, M. J., J. S. Delamere, E. J. Mlawer, M. W. Shephard, S. A. Clough, and W. D. Collins, 2008: Radiative forcing by long-lived greenhouse gases: Calculations with the AER radiative transfer models. *J. Geophys. Res.*, **113**, D13103, https://doi.org/10.1029/2008JD009944.

Ikuta, Y., and Y. Honda, 2011: Development of 1D+4DVAR data assimilation of radar reflectivity in JnoVA. *CAS/JSC WGNE Res. Act. Atmos. Oceanic Modell.*, **41**, 1–9.

Jones, T. A., X. Wang, P. Skinner, A. Johnson, and Y. Wang, 2018: Assimilation of *GOES-13* imager clear-sky water vapor (6.5 μm) radiances into a Warn-on-Forecast System. *Mon. Wea. Rev.*, **146**, 1077–1107, https://doi.org/10.1175/MWR-D-17-0280.1.

Kawabata, T., T. Schwitalla, A. Adachi, H.-S. Bauer, V. Wulfmeyer, N. Nagumo, and H. Yamauchi, 2018: Observational operators for dual polarimetric radars in variational data assimilation systems (PolRad VAR v1.0). *Geosci. Model Dev.*, **11**, 2493–2501, https://doi.org/10.5194/gmd-11-2493-2018.

Krause, J. M., and V. Klaus, 2023: Identifying updrafts with ZDR hotspots. *40th Conf. on Radar Meteorology*, Minneapolis, MN, Amer. Meteor. Soc., 13A.4, https://ams.confex.com/ams/40RADAR/meetingapp.cgi/Paper/426068.

Kumjian, M. R., 2013a: Principles and applications of dual-polarization weather radar. Part I: Description of the polarimetric radar variables. *J. Oper. Meteor.*, **1**, 226–242, https://doi.org/10.15191/nwajom.2013.0119.

——, 2013b: Principles and applications of dual-polarization weather radar. Part II: Warm- and cold-season applications. *J. Oper. Meteor.*, **1**, 243–264, https://doi.org/10.15191/nwajom.2013.0120.

——, A. P. Khain, N. Benmoshe, E. Ilotoviz, A. V. Ryzhkov, and V. T. J. Phillips, 2014: The anatomy and physics of Z_{DR} columns: Investigating a polarimetric radar signature with a spectral bin model. *J. Appl. Meteor. Climatol.*, **53**, 1820–1843, https://doi.org/10.1175/JAMC-D-13-0354.1.

Lai, A., J. Gao, S. E. Koch, Y. Wang, S. Pan, A. O. Fierro, C. Cui, and J. Min, 2019: Assimilation of radar radial velocity, reflectivity, and pseudo–water vapor for convective-scale NWP in a variational framework. *Mon. Wea. Rev.*, **147**, 2877–2900, https://doi.org/10.1175/MWR-D-18-0403.1.

Li, X., and J. R. Mecikalski, 2010: Assimilation of the dual-polarization Doppler radar data for a convective storm with a warm-rain radar forward operator. *J. Geophys. Res.*, **115**, D16208, https://doi.org/10.1029/2009JD013666.

——, and ——, 2012: Impact of the dual-polarization Doppler radar data on two convective storms with a warm-rain radar forward operator. *Mon. Wea. Rev.*, **140**, 2147–2167, https://doi.org/10.1175/MWR-D-11-00090.1.

——, ——, and D. Posselt, 2017: An ice-phase microphysics forward model and preliminary results of polarimetric radar data assimilation. *Mon. Wea. Rev.*, **145**, 683–708, https://doi.org/10.1175/MWR-D-16-0035.1.

Posselt, D. J., X. Li, S. A. Tushaus, and J. R. Mecikalski, 2015: Assimilation of dual-polarization radar observations in mixed- and ice-phase regions of convective storms: Information content and forward model errors. *Mon. Wea. Rev.*, **143**, 2611–2636, https://doi.org/10.1175/MWR-D-14-00347.1.

Roberts, N. M., and H. W. Lean, 2008: Scale-selective verification of rainfall accumulations from high-resolution forecasts of convective events. *Mon. Wea. Rev.*, **136**, 78–97, https://doi.org/10.1175/2007MWR2123.1.

Roebber, P. J., 2009: Visualizing multiple measures of forecast quality. *Wea. Forecasting*, **24**, 601–608, https://doi.org/10.1175/2008WAF2222159.1.

Skamarock, W. C., and J. B. Klemp, 2008: A time-split nonhydrostatic atmospheric model for weather research and forecasting applications. *J. Comput. Phys.*, **227**, 3465–3485, https://doi.org/10.1016/j.jcp.2007.01.037.

Smith, T. L., S. G. Benjamin, J. M. Brown, S. Weygandt, T. Smirnova, and B. Schwartz, 2008: Convection forecasts from the hourly updated, 3-km High Resolution Rapid Refresh (HRRR) model. *24th Conf. on Severe Local Storms*, Savannah, GA, Amer. Meteor. Soc., 11.1, https://ams.confex.com/ams/pdfpapers/142055.pdf.

Snyder, J. C., A. V. Ryzhkov, M. R. Kumjian, A. P. Khain, and J. Picca, 2015: A Z_{DR} column detection algorithm to examine convective storm updrafts. *Wea. Forecasting*, **30**, 1819–1844, https://doi.org/10.1175/WAF-D-15-0068.1.

Sun, J., and N. A. Crook, 1997: Dynamical and microphysical retrieval from Doppler radar observations using a cloud model and its adjoint. Part I: Model development and simulated data experiments. *J. Atmos. Sci.*, **54**, 1642–1661, https://doi.org/10.1175/1520-0469(1997)054<1642:DAMRFD>2.0.CO;2.

——, and A. N. Crook, 1998: Dynamical and microphysical retrieval from Doppler radar observations using a cloud model and its adjoint. Part II: Retrieval experiments of an observed Florida convective storm. *J. Atmos. Sci.*, **55**, 835–852, https://doi.org/10.1175/1520-0469(1998)055<0835:DAMRFD>2.0.CO;2.

——, and Coauthors, 2014: Use of NWP for nowcasting convective precipitation: Recent progress and challenges. *Bull. Amer. Meteor. Soc.*, **95**, 409–426, https://doi.org/10.1175/BAMS-D-11-00263.1.

Thompson, G., P. R. Field, R. M. Rasmussen, and W. D. Hall, 2008: Explicit forecasts of winter precipitation using an improved bulk microphysics scheme. Part II: Implementation of a new snow parameterization. *Mon. Wea. Rev.*, **136**, 5095–5115, https://doi.org/10.1175/2008MWR2387.1.

Tong, M., and M. Xue, 2005: Ensemble Kalman filter assimilation of Doppler radar data with a compressible nonhydrostatic model: OSS experiments. *Mon. Wea. Rev.*, **133**, 1789–1807, https://doi.org/10.1175/MWR2898.1.

van Lier-Walqui, M., and Coauthors, 2016: On polarimetric radar signatures of deep convection for model evaluation: Columns of specific differential phase observed during MC3E. *Mon. Wea. Rev.*, **144**, 737–758, https://doi.org/10.1175/MWR-D-15-0100.1.

Wang, H., J. Sun, S. Fan, and X.-Y. Huang, 2013: Indirect assimilation of radar reflectivity with WRF 3D-Var and its impact on prediction of four summertime convective events. *J. Appl. Meteor. Climatol.*, **52**, 889–902, https://doi.org/10.1175/JAMC-D-12-0120.1.

——, and Coauthors, 2018: Incorporating geostationary lightning data into a radar reflectivity based hydrometeor retrieval method: An observing system simulation experiment. *Atmos. Res.*, **209**, 1–13, https://doi.org/10.1016/j.atmosres.2018.03.002.

Wang, Y., and X. Wang, 2017: Direct assimilation of radar reflectivity without tangent linear and adjoint of the nonlinear observation operator in the GSI-based EnVar system: Methodology and experiment with the 8 May 2003 Oklahoma City tornadic supercell. *Mon. Wea. Rev.*, **145**, 1447–1471, https://doi.org/10.1175/MWR-D-16-0231.1.

——, J. Gao, P. S. Skinner, K. Knopfmeier, T. Jones, G. Creager, P. L. Heiselman, and L. J. Wicker, 2019: Test of a weather-adaptive dual-resolution hybrid warn-on-forecast analysis and forecast system for several severe weather events. *Wea. Forecasting*, **34**, 1807–1827, https://doi.org/10.1175/WAF-D-19-0071.1.

Wattrelot, E., O. Caumont, and J.-F. Mahfouf, 2014: Operational implementation of the 1D+3D-Var assimilation method of radar reflectivity data in the AROME model. *Mon. Wea. Rev.*, **142**, 1852–1873, https://doi.org/10.1175/MWR-D-13-00230.1.

Xiao, Q., Y.-H. Kuo, J. Sun, W.-C. Lee, D. M. Barker, and E. Lim, 2007: An approach of radar reflectivity data assimilation and its assessment with the inland QPF of Typhoon Rusa (2002) at landfall. *J. Appl. Meteor. Climatol.*, **46**, 14–22, https://doi.org/10.1175/JAM2439.1.

Xue, M., M. Tong, and K. K. Droegemeier, 2006: An OSSE framework based on the ensemble square root Kalman filter for evaluating the impact of data from radar networks on thunderstorm analysis and forecasting. *J. Atmos. Oceanic Technol.*, **23**, 46–66, https://doi.org/10.1175/JTECH1835.1.

——, Y. Jung, and G. Zhang, 2010: State estimation of convective storms with a two-moment microphysics scheme and an ensemble Kalman filter: Experiments with simulated radar data. *Quart. J. Roy. Meteor. Soc.*, **136**, 685–700, https://doi.org/10.1002/qj.593.

Zhang, G., and Coauthors, 2019: Current status and future challenges of weather radar polarimetry: Bridging the gap between radar meteorology/hydrology/engineering and numerical weather prediction. *Adv. Atmos. Sci.*, **36**, 571–588, https://doi.org/10.1007/s00376-019-8172-4.

——, J. Gao, and M. Du, 2021: Parameterized forward operators for simulation and assimilation of polarimetric radar data with numerical weather predictions. *Adv. Atmos. Sci.*, **38**, 737–754, https://doi.org/10.1007/s00376-021-0289-6.